Journal of Medicinal Chemistry

pubs.acs.org/jmc

Article

Exploring the Effect of Halogenation in a Series of Potent and Selective A_{2B} Adenosine Receptor Antagonists

Rubén Prieto-Díaz, Manuel González-Gómez, Hugo Fojo-Carballo, Jhonny Azuaje, Abdelaziz El Maatougui, Maria Majellaro, María I. Loza, José Brea,* Víctor Fernández-Dueñas, M. Rita Paleo, Alejandro Díaz-Holguín, Beatriz Garcia-Pinel, Ana Mallo-Abreu, Juan C. Estévez, Antonio Andújar-Arias, Xerardo García-Mera, Iria Gomez-Tourino, Francisco Ciruela, Cristian O. Salas, Hugo Gutiérrez-de-Terán,* and Eddy Sotelo*

Cite This: *J. Med. Chem.* 2023, 66, 890−912

Read Online

ACCESS | Metrics & More | Article Recommendations | Supporting Information

ABSTRACT: The modulation of the A_{2B} adenosine receptor is a promising strategy in cancer (immuno) therapy, with A_{2B}AR antagonists emerging as immune checkpoint inhibitors. Herein, we report a systematic assessment of the impact of (di- and mono-)halogenation at positions 7 and/or 8 on both A_{2B}AR affinity and pharmacokinetic properties of a collection of A_{2B}AR antagonists and its study with structure-based free energy perturbation simulations. Monohalogenation at position 8 produced potent A_{2B}AR ligands irrespective of the nature of the halogen. In contrast, halogenation at position 7 and dihalogenation produced a halogen-size-dependent decay in affinity. Eight novel A_{2B}AR ligands exhibited remarkable affinity (K_i < 10 nM), exquisite subtype selectivity, and enantioselective recognition, with some eutomers eliciting sub-nanomolar affinity. The pharmacokinetic profile of representative derivatives showed enhanced solubility and microsomal stability. Finally, two compounds showed the capacity of reversing the antiproliferative effect of adenosine in activated primary human peripheral blood mononuclear cells.

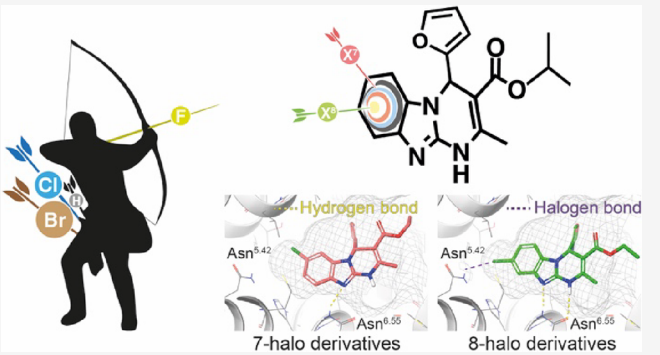

INTRODUCTION

Adenosine (Ado) is an essential signaling nucleoside that is either released from cells or extracellularly generated, by sequential hydrolysis of adenosine 5′-triphosphate and adenosine 5′-monophosphate by the ectonucleotidases CD39 and CD73.[1] Ado is ubiquitous in mammalian cells, being a key intermediate metabolite that modulates several biochemical processes,[2,3] ranging from energy transfer, signal transduction, sleep−wake cycle,[4] inflammation,[5] to immunity.[6,7] In healthy tissues, the extracellular concentration of Ado is generally low, although it can increase rapidly from nanomolar to micromolar,[1] which contributes to the protection of tissues against damage caused by stress, injury, hypoxia, or inflammation.[3,8,9] Four rhodopsin-like G protein-coupled receptors (GPCRs) sense the extracellular Ado levels, constituting the class 1 purinergic receptors (P_1) A_1AR, A_{2A}AR, A_{2B}AR, and A_3AR. Each adenosine receptor (AR) subtype has unique sequence homology, tissue distribution, second messenger coupling, and pharmacology.[8] The physiology of Ado signaling through these receptors and its pathophysiological implications in human diseases have been recently reviewed.[1]

A_{2B}AR remains the most puzzling and poorest-characterized AR subtype.[10] Ubiquitously expressed but usually at low levels (except at human cecum, large intestine, mast cells, and hematopoietic cells), A_{2B}AR displays the lowest affinity for Ado among all four subtypes (30−300 nM), remaining silent in healthy conditions.[1] Such a behavior, together with its high structural homology with the well-characterized A_{2A}AR, led to the initial perception that A_{2B}AR would have only minor physiological relevance. However, it is now well documented that A_{2B}AR becomes activated under particular pathological conditions such as hypoxia, inflammation, infection, and cancer, where extracellular Ado levels are increased up to micromolar concentrations, consequently increasing attention to the therapeutic potential of A_{2B}AR as a drug target.[11] A_{2B}AR antagonists have been recently proposed as potential drugs for

Received: October 31, 2022
Published: December 14, 2022

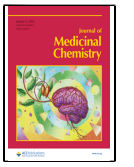

https://doi.org/10.1021/acs.jmedchem.2c01768
J. Med. Chem. 2023, 66, 890−912

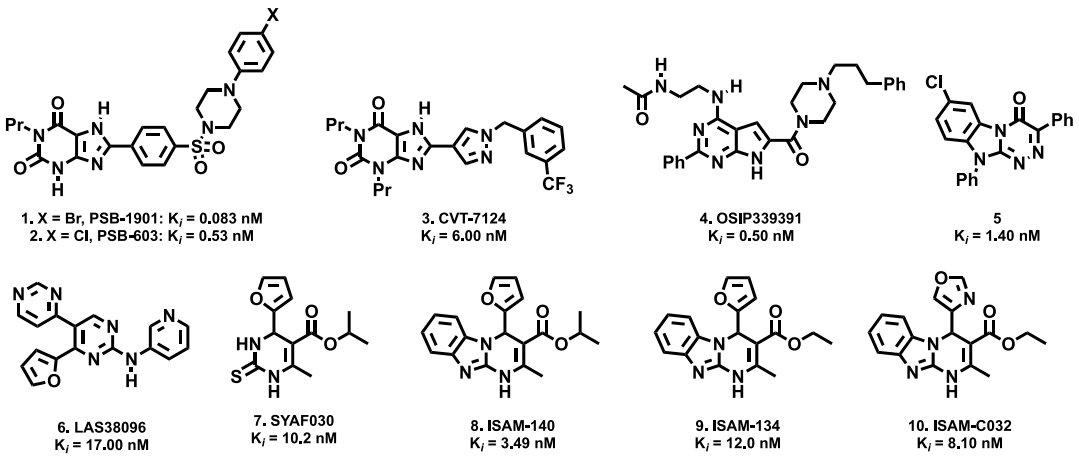

Figure 1. Structure of representative potent and selective A_{2B} antagonists.

the treatment of inflammation, diabetes, pain, asthma, and Alzheimer disease.[12−15] More recent is the identification of A_{2B}AR as an important player to different facets of cancer progression, e.g., tumor growth, metastasis, and angiogenesis.[16,17] Advances in cancer immunotherapy highlight the importance of Ado as a key metabolite that suppresses antitumor immune response by T and NK cells in the tumor microenvironment,[18] this immune role being specifically mediated by A_{2A} and A_{2B} ARs.[19−21] Indeed, several A_{2A}AR antagonists are under clinical trials as immune checkpoint inhibitors for the treatment of different cancer types.[22] A_{2A}AR and A_{2B}AR exhibit high homology and are often co-expressed on cells.[23] Recent studies suggested formation of heteromeric A_{2A}AR−A_{2B}AR complexes and revealed that ligand recognition, signaling, and pharmacology of A_{2A}AR are blocked by A_{2B}AR.[24] According to all this evidence, A_{2B}AR antagonists and dual A_{2A}AR-A_{2B}AR antagonists are emerging as effective cancer (immuno)therapeutics, where the consequent reactivation of the immune system results in antiproliferative, antiangiogenic, and antimetastatic effects.[25,26]

The therapeutic opportunities arising from A_{2B}AR modulation have driven the development of A_{2B}AR antagonists. The naturally occurring xanthine derivatives (e.g., caffeine and theophylline) early inspired the discovery and optimization of xanthine congeners and structurally related deaza analogues and purine derivatives.[27] Xanthines have been intensively studied, allowing the identification of derivatives eliciting optimal affinity−selectivity profiles (Figure 1, Cmpds **1**−**4**), being so far the most widely explored A_{2B}AR antagonists.[28] However, their challenging physicochemical features and pharmacokinetic (PK) profiles remain as the major drawback of this chemotype to advance further on the drug discovery pipeline. Consequently, recent efforts have been focused on the development of non-xanthinic A_{2B}AR antagonists (Figure 1, Cmpds **5**−**10**).[29−32] In this context, we have reported novel series of pyrimidine-based ligands (Figure 1, Cmpds **7**−**10**), which encompass structural novelty, exquisite affinity and selectivity, and excellent synthetic feasibility.[29−31] A hybrid approach, combining scaffold hopping and thorough SAR investigation, have guided the expansion of these series. Importantly, these compounds contain a chiral center within the heterocyclic core (Figure 1, Cmpds **7**−**10**), offering a novel structural element as compared to classical, planar A_{2B}AR antagonists. Consequent racemate separation provided the first examples of antagonists with enantiospecific A_{2B}AR recognition.[25,31,33−35]

In the frame of an optimization program of non-xanthine A_{2B}AR antagonists as promising cancer (immuno)-therapeutics,[25,36] we determined to analyze the impact of di- and mono-halogenation at positions 7 and 8 of the tricyclic core of prototypical A_{2B}AR antagonists (Figure 1, Cmpds **8**−**10**).[30,31] The main goal was to improve the pharmacodynamic and PK profiles of this chemotype, while maintaining (or even improving) the affinity and selectivity profiles. The phenyl ring of the tricyclic system is the most easily metabolizable part, only next to the exocyclic pentagonal ring that was already optimized in a previous work,[31] and halogenation arises as a strategy to reduce the probability of intensive metabolization. At the same time, the size variability of halogen substitution would allow a deeper exploration of the interactions proposed by earlier modeling studies in the internal cavity of A_{2B}AR.[29−31] The synthesis and pharmacological characterization of a collection of 80 novel tricyclic ligands is here assessed by free energy perturbation (FEP) simulations, evidencing the superior profile of 8-halo derivatives by optimizing interactions with the modeled binding site. This study further confirms the previously modeled enantiospecific A_{2B}AR recognition of the pentagonal ring at position 4, and the antagonist profile of the most promising compounds. In addition, examination of the ADMET profile of representative antagonists confirmed that the introduction of a fluorine atom improves solubility and microsomal stability. Two of the ligands here optimized were selected to investigate the effect of A_{2B}AR antagonism on immune cell proliferation, demonstrating that the ligands reverse the reduction of Ado-related proliferation in human primary immune cells.

RESULTS AND DISCUSSION

Design. These novel series were conceived in the context of our ongoing projects to develop multi-target cancer (immuno)therapeutics and PET tracers for A_{2B}AR, starting from the scaffold of ISAM-140 (Figure 1) as a prototype ligand. Introduction of functional groups at positions 7 and 8 of the heterotricyclic core evidenced conspicuous effects on the affinity and selectivity profile, thus inspiring the design of the present series. It was anticipated that halogenation at positions 7 and 8 of the phenyl ring within the tricyclic core would not only result in compounds with improved pharmacodynamic

https://doi.org/10.1021/acs.jmedchem.2c01768
J. Med. Chem. 2023, 66, 890−912

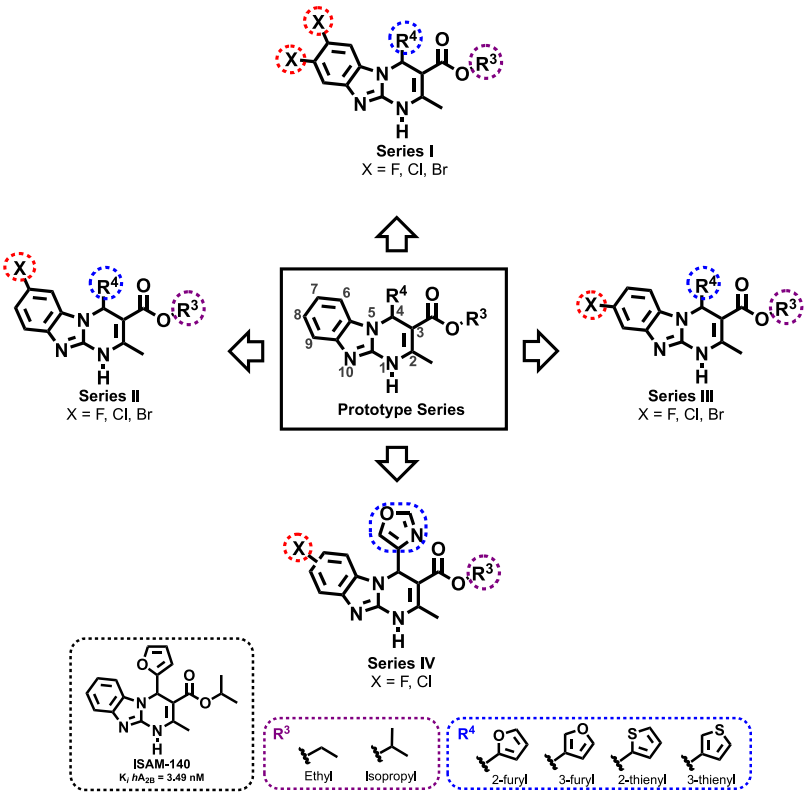

Figure 2. Design strategy and diversity elements explored during the study.

and PK profiles but also provide valuable data to understand the molecular basis behind the observed SAR trends.

Thus, we envisioned the development of the 80 new ligands (series **I**–**IV**) presented in Figure 2. Being aware that the impact of halogenation on binding affinity and selectivity might be position-dependent and that it can heavily rely on the nature of the halogen, we systematically introduced F, Cl, and Br atoms at positions 7 and 8 of the tricyclic scaffold (Figure 2). To preserve consistency from the early series and facilitate the comparative SAR, the herein obtained ligands (series **I**–**IV**) retained the structural elements that provided optimal A_{2B}AR affinity at positions 3 and 4 (Figure 2). Thus, for R^4, we initially considered a set of four pentagonal heteroaryl groups (2-furyl, 3-furyl, 2-thienyl, 3-thienyl), while the alkoxy residues of the ester moiety (R^3) consist of either ethyl or isopropyl groups. Three series were subsequently conceived, each consisting of 24 derivatives (Figure 2 and Tables 2–4). Series **I** contain two identical halogen atoms at positions 7 and 8 (compounds **14a**–**x**), whereas in series **II** and **III** (monohalogenated), the halogen atom is present in position 7 or 8 respectively (compounds **15a**–**x** and **16a**–**x**). Finally, a focused series consisted of eight 7-halo or 8-halo derivatives bearing a 4-oxazolyl group (Table 5), which we have recently identified as an optimal non-furan pentagonal nucleus for position 4.[31] This limited series was obtained by prioritizing two halogens (F and Cl) and the substitution patterns that provided better affinity and selectivity profiles in series **I**–**III**.

Chemistry. The halogenated alkyl 4-heteroaryl-2-methyl-1,4-dihydrobenzo[4,5]-imidazo[1,2-*a*]pyrimidine-3-carboxylates (**14**–**18**) were obtained as depicted in Scheme 1. A three-component synthesis, based on the robust and efficient Biginelli reaction (i.e., the three-component reaction of an aldehyde, a *β*-ketoester, and 1,3-dinucleophiles), enabled a time- and cost-effective assembly of the large collection obtained. A set of pentagonal carbaldehydes (**12a**–**e**) and *β*-ketoesters (**13a**,**b**) providing optimal substituents for positions 4 and 3 in combination with six halogenated 2-amino-benzimidazoles (**11a**–**f**) were employed as precursors. The starting materials, dissolved in THF and containing a catalytic amount of $ZnCl_2$ (or acetic acid), were submitted to orbital stirring at 90 °C (12 h) or microwave radiation at 80 °C (90 min). The targeted tricyclic derivatives were obtained in moderate to satisfactory yields (30–85%). For the synthesis of a series of monohalogenated (7-halo or 8-halo) derivatives (Scheme 1, Cmpds **15**–**18**), the corresponding 2-amino-5-halobenzimidazoles (**11d**–**f**) were employed as precursors. The phenomenon of tautomerization enabled to directly obtain the targeted (7- or 8-)halogenated alkyl 4-heteroaryl-2-methyl-1,4-dihydrobenzo-[4,5]imidazo[1,2-*a*]pyrimidine-3-carboxylates as regioisomeric mixtures in a 1:1 ratio. Both regioisomers (series **II** and **III**) were isolated in pure forms after chromatographic separation. All reactions were monitored by thin-layer chromatography (TLC). After completion of the reaction, the solvent was evaporated to dryness and the isolated solid was purified by column chromatography on silica gel. A detailed description of the synthetic methods and the complete structural, spectroscopic, and analytical data for all compounds are provided in the experimental part. Unambiguous structural characterization of each regioisomer has been carried out with a combination of X-ray crystallography and 2D-NMR experiments (Scheme 1). The monohalogenated compounds (series **II**–**IV**) differ in the position of the halogen atom located at either C7 or C8. Both regioisomers present an ABX aromatic substitution pattern in the ^{1}H NMR (Scheme 1). X-ray diffraction analysis of **16s** (see the Supporting Information) shows that protons H4 (alpha hydrogen to the

https://doi.org/10.1021/acs.jmedchem.2c01768
J. Med. Chem. 2023, 66, 890–912

Scheme 1. Biginelli-Based Synthesis. Method (A) $ZnCl_2$, THF, 90 °C, 12 h. Method (B) AcOH, THF/DMF (2:1), 80 °C, MW, 90 min; and Regioisomer Characterization Strategy (in Red: Signal with NOE Effect Irradiating H_4)

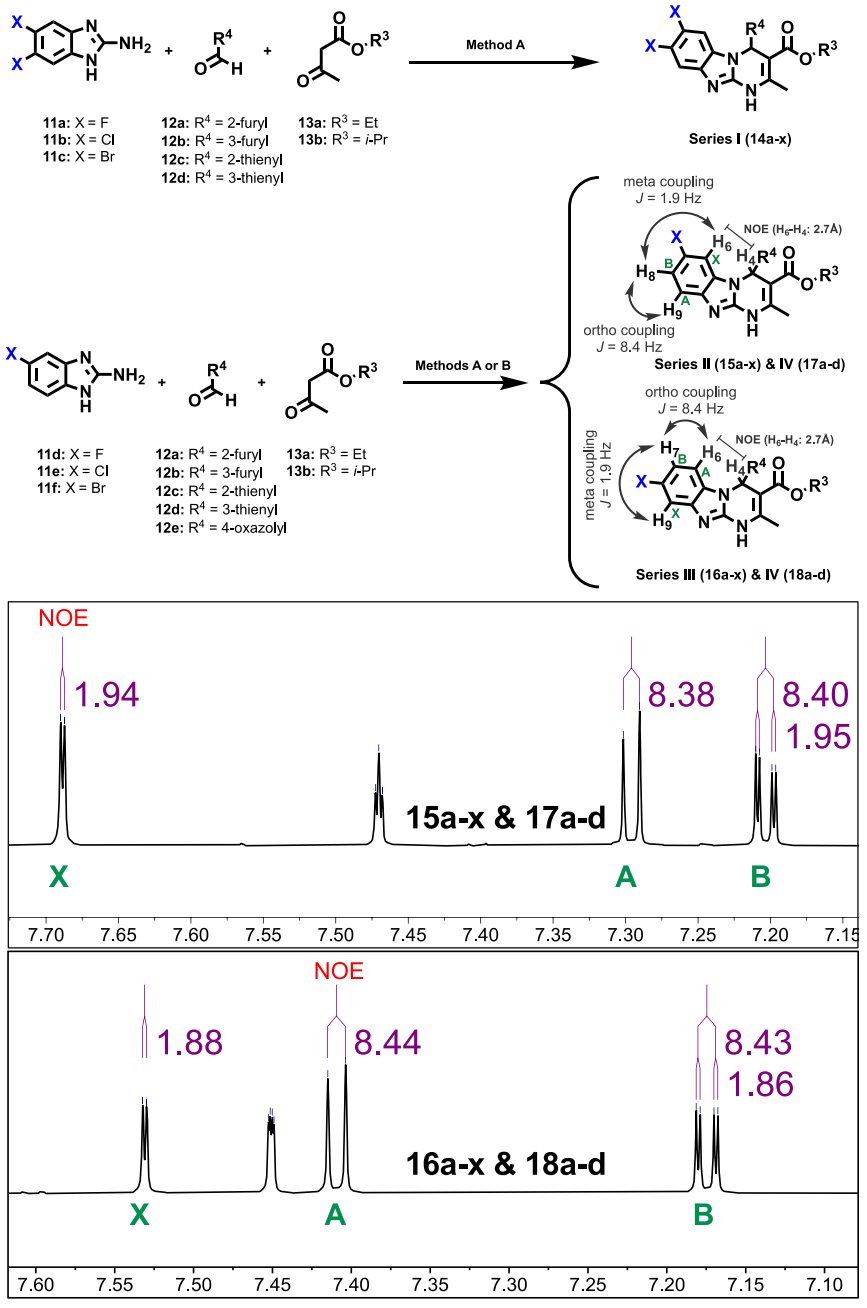

five-membered ring) and H6 (aromatic proton) are 2.7 Å apart, allowing us to perform NOE experiments (Supplementary Figure S1). The 2D-ROESY NMR spectrum of **16s** (Supplementary Figure S1A) showed a correlation of H4 (singlet, δ 6.60 ppm) and the doublet (J = 8.4 Hz) at δ 7.41 ppm corresponding to H6. The coupling constant value is typical of H−H *ortho* coupling and indicates the presence of a hydrogen in C7 and therefore of the halogen at C8. However, the 2D-ROESY NMR spectrum of **15s** (Supplementary Figure S1B) showed a correlation between H4 (singlet at δ 6.53 ppm) and H6 (doublet at δ 7.70 ppm). The coupling constant value, J = 1.9 Hz, indicates a H−H *meta* coupling, and thus the halogen is in the *ortho* position (C7). Similar correlations were observed for other pairs of regioisomers (Supplementary Figure S2). As in previous series (Figure 1 and Table 1, compounds **7**−**10**), all ligands obtained in this study contain one stereocenter at position 4 of the heterocyclic core and were isolated and evaluated as racemic mixtures. Six ligands eliciting an attractive A_{2B}AR affinity/selectivity profile were submitted to chiral resolution to isolate its corresponding enantiomer pairs.

Biological Evaluation. The adenosinergic profile (affinity and selectivity) of the 80 novel halogenated alkyl 1,4-dihydrobenzo[4,5]imidazo[1,2-*a*]pyrimidine-3-carboxy-lates was evaluated in vitro using radioligand binding assays at the four human AR subtypes.[30,31,33,34] Tables 2−5 contain the binding data obtained, while, to facilitate the comparative assessment, Table 1 shows the binding data for the prototype series.[30] All ligands reported in Tables 1−5 were obtained and tested as racemic mixtures. The whole set was evaluated in silico with a

https://doi.org/10.1021/acs.jmedchem.2c01768
J. Med. Chem. 2023, 66, 890−912

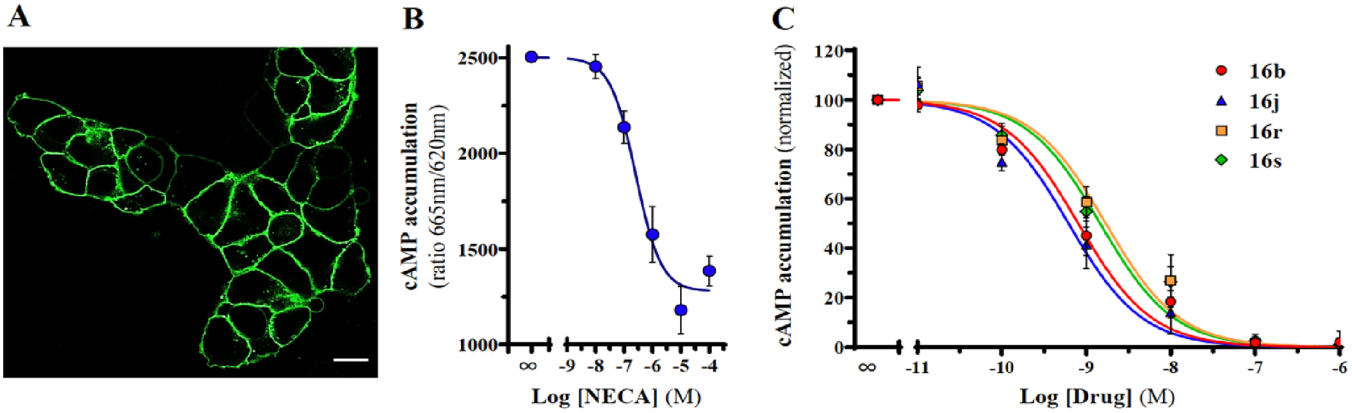

Figure 3. Blockade of A_{2B}AR-mediated cAMP accumulation. (A) HEK-293 cells permanently expressing the $A_{2B}AR^{SNAP}$ construct were stained with the fluorescent SNAP-488 substrate and visualized using a confocal microscope.[38] Scale bar: 10 μM. (B) Determination of NECA-mediated cAMP accumulation in $A_{2B}AR^{SNAP}$ cells. Cells were incubated in the absence or presence of increasing concentrations of NECA, and the cAMP accumulation determined as described in Experimental Section. The straight TR-FRET signal (ratio 665 nm/620 nm) of the assay is shown. (C) cAMP accumulation in $A_{2B}AR^{SNAP}$ cells stimulated with NECA (1 μM) in the absence or presence of increasing concentrations of **16b**, **16j**, **16r**, and **16s**. Data are expressed as mean ± SEM (n = 4).

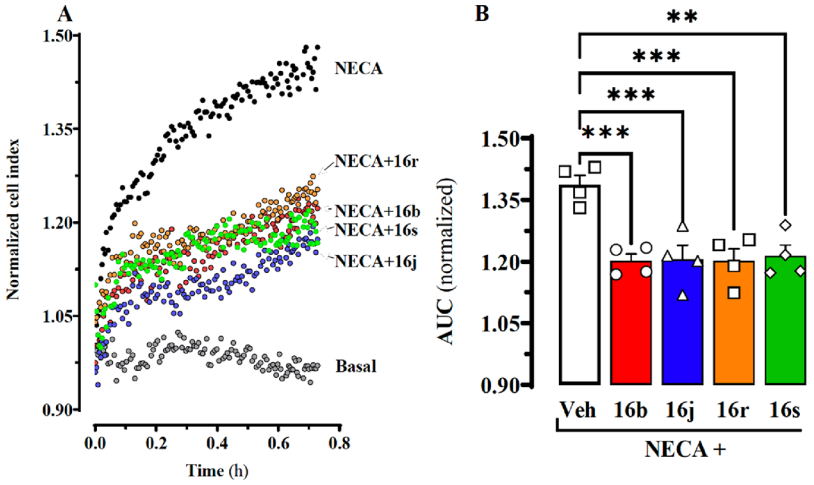

Figure 4. Blockade of A_{2B}AR-mediated whole-cell label-free responses. (A) Representative example of the impedance signal obtained over the time upon incubation with A_{2B}AR ligands. Cells were stimulated with vehicle or NECA (1 μM) in the absence or presence of **16b**, **16j**, **16r**, and **16s** (1 μM), 18 h after seeding, and the impedance signal recorded in real-time during 45 min. (B) The area under the curve (AUC) derived from the normalized cell index (NCI) shown in (A) was calculated for each condition. Data are expressed as mean ± SEM (n = 4). ***P < 0.001 and **P < 0.01, one-way ANOVA with a Dunnett's multiple-comparison test when compared to vehicle (Veh).

combination of a Rdkit[37] PAINS filter and Instant JChem from Chemaxon (https://www.chemaxon.com), to rule out the possibility that these ligands can be promiscuous pan-assay interference compounds (PAINS) and to assess their bioavailability, respectively. Human ARs were expressed in transfected cell lines [e.g., Chinese hamster ovary (CHO) cells (A_1AR), human epithelial carcinoma (HeLa) cells (A_{2A}AR and A_3AR), and human embryonic kidney (HEK-293) cells (A_{2B}AR)]. [^{3}H]DPCPX for A_1AR and A_{2B}AR, [^{3}H]NECA for A_3AR, and [^{3}H]ZM241385 for A_{2A}AR were employed as radioligands. The binding data is presented as K_i ± SEM (nM, n = 3) obtained by fitting the data by non-linear regression using Prism 5.0 software (GraphPad, San Diego, California), or as specific binding inhibition percentage at 1 μM (n = 2, average) for those compounds that did not completely displace the radioligand due to either little affinity or poor solubility. The binding affinity of reference AR ligands (ISAM-140, DPCPX, NECA, and ZM241385) was assessed using our experimental protocols and reported in Tables 1−5 for comparison. The stereoisomers of selected compounds were obtained by chiral resolution and tested at the four human AR subtypes in their enantiopure forms (Table 6). This data was employed to complement the SAR study and to evaluate the importance of the configuration of the stereogenic center on the affinity.

Intrinsic Activity Assays. Four representative ligands (**16b**, **16j**, **16r**, and **16s**) were selected to gain insight into the functional effect of the obtained series. To assess their ability to block A_{2B}AR agonist intrinsic activity, the effect on A_{2B}AR-mediated cAMP accumulation and cellular impedance was evaluated. To this end, we used HEK-293 cells permanently expressing the $A_{2B}AR^{SNAP}$ construct, which can be visualized upon staining the cells with a SNAP-fluorescent substrate. As shown in Figure 3A, $A_{2B}AR^{SNAP}$ nicely decorated the cell surface of $A_{2B}AR^{SNAP}$ cells, indicating that the receptor was readily expressed at the plasma membrane. Subsequently, we evaluated the effect of **16b**, **16j**, **16r**, and **16s** in A_{2B}AR signaling by monitoring cAMP accumulation in $A_{2B}AR^{SNAP}$

https://doi.org/10.1021/acs.jmedchem.2c01768
J. Med. Chem. 2023, 66, 890−912

Table 1. Structure and Adenosine Receptor Affinities of Alkyl 1,4-Dihydrobenzo [4,5]imidazo[1,2-*a*]pyrimidine-3-carboxylates (Prototype Series)[30,31]

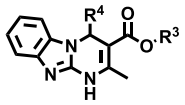

			K_i (nM) or % at 1 μM			
compound	R^4	R^3	hA_1[a]	hA_{2A}[b]	hA_{2B}[c]	hA_3[d]
I (ISAM-134)	2-furyl	Et	5%	14%	12.0 ± 0.7	1%
II (ISAM-140)	2-furyl	*i*-Pr	20%	28%	3.49 ± 0.2	2%
III (ISAM-141)	3-furyl	Et	7%	11%	20.6 ± 1.1	1%
IV (ISAM-142)	3-furyl	*i*-Pr	12%	23%	11.4 ± 0.5	2%
V	2-thienyl	Et	8%	16%	484 ± 3	1%
VI	2-thienyl	*i*-Pr	1%	17%	371 ± 5	3%
VII	3-thienyl	Et	3%	10%	29.7 ± 1.2	2%
VIII	3-thienyl	*i*-Pr	11%	3%	29.34 ± 1.1	21%
IX (ISAM-C032)	4-oxazolyl	Et	5%	11%	8.10 ± 0.5	7%
X	4-oxazolyl	*i*-Pr	7%	19%	43.4 ± 1.3	16%
DPCPX			2.20 ± 0.2	157 ± 3	73.2 ± 1.4	1722 ± 11
ZM241385			683 ± 4	1.9 ± 0.1	65.7 ± 1.1	863 ± 4
NECA			14.0 ± 1	20.0 ± 3	2400 ± 35	6.20 ± 0.9

[a]Displacement of specific [^{3}H]DPCPX binding in human CHO cells expressed as K_i in nanomolars (n = 3) or percentage displacement of specific binding at a concentration of 1 μM (n = 2). [b]Displacement of specific [^{3}H]4-(2-[7-amino-2-(2-furyl)[1,2,4]triazolo[2,3-*a*][1,3,5]triazin-5-ylamino]ethyl)phenol binding in human HeLa cells expressed as K_i in nanomolars (n = 3) or percentage displacement of specific binding at a concentration of 1 μM (n = 2). [c]Displacement of specific [^{3}H]DPCPX binding in human HEK-293 cells expressed as K_i in nanomolars (n = 3) or percentage displacement of specific binding at a concentration of 1 μM (n = 2). [d]Displacement of specific [^{3}H]NECA binding in human HeLa cells expressed as K_i in nanomolars (n = 3) or percentage displacement of specific binding at a concentration of 1 μM (n = 2).

cells treated with NECA, a non-selective Ado receptor agonist. NECA induced a concentration-dependent cAMP accumulation in $A_{2B}AR^{SNAP}$ cells with an EC_{50} of 257 ± 94 nM (Figure 3B). Subsequently, $A_{2B}AR^{SNAP}$ cells were evaluated with a fixed concentration of NECA (1 μM) in the absence or presence of increasing concentrations of **16b**, **16j**, **16r**, and **16s** and the K_B value for each compound was calculated, namely, 0.8 ± 0.2, 0.6 ± 0.2, 1.7 ± 0.6, and 1.5 ± 0.5 nM, respectively (Figure 3C). Overall, **16b**, **16j**, **16r**, and **16s** displayed low nanomolar potency while blocking $A_{2B}AR$-mediated cAMP accumulation in $A_{2B}AR^{SNAP}$ cells, thus indicating an antagonist intrinsic activity nature. Comparative K_B and K_i data for selected compounds is shown in Table 7. It should be noticed that two these selective $A_{2B}AR$ antagonists exhibit sub-nanomolar K_B data.

To further evaluate the ability of **16b**, **16j**, **16r**, and **16s** to preclude $A_{2B}AR$ function in living cells, we took advantage of the cellular impedance label-free method, a widely accepted morphological and functional biosensor of cell status.[39] Accordingly, whole-cell NECA-mediated impedance responses of $A_{2B}AR^{SNAP}$ cells were monitored in real time in the absence or presence of **16b**, **16j**, **16r**, and **16s**. Indeed, NECA (1 μM) induced a significant increase in $A_{2B}AR^{SNAP}$ cell impedance recordings, thus reflecting changes in cell morphology upon agonist challenge (Figure 4A). Importantly, **16b**, **16j**, **16r**, and **16s** partially blocked the NECA-induced impedance increase in $A_{2B}AR^{SNAP}$ cells (Figure 4A). When calculating the area under the curve (AUC) for the different experimental conditions, we can observe that **16b**, **16j**, **16r**, and **16s** significantly blocked NECA-induced changes in cellular impedance (Figure 4B). These results from an alternative cellular functional assay further confirmed that **16b**, **16j**, **16r**, and **16s** were able to block $A_{2B}AR$ agonist-mediated intrinsic activity.

Interestingly, the absolute **16b**, **16j**, **16r**, and **16s** antagonist potencies in the cAMP accumulation assay were greater (~10-fold) than those determined in the radioligand binding assays, a fact that has been previously reported in HEK-293 cells stably overexpressing $A_{2B}AR$.[40] Indeed, this notion can be supported by the spare receptor theory defining that under some circumstances, the potency of a named agonist in functional assays is proportional to the receptor density, thus producing a discontinuity between drug occupancy and cell response.[41] Our label-free experiments revealed a significant, but partial, blockade of a NECA-induced impedance increase in $A_{2B}AR^{SNAP}$ cells. Indeed, HEK-293 cells express endogenous Ado receptors as revealed by microarray analysis.[42] Thus, while A_3AR was not detected, the remaining $A_{2B}AR$, $A_{2A}AR$, and A_1AR were identified in HEK-293 cells.[42] Since NECA is a non-selective Ado receptor agonist showing affinity for $A_{2A}AR$ and A_1AR (K_i values of 20 and 14 nM, respectively),[43] it can be speculated that the remaining impedance increase in NECA-treated $A_{2B}AR^{SNAP}$ cells in the presence of **16b**, **16j**, **16r**, and **16s** can be mediated by endogenous A_{2A} and A_1 ARs. These results might be interpreted as indirect evidence of selectivity for the $A_{2B}AR$ for compounds **16b**, **16j**, **16r**, and **16s**.

Structure–Activity Relationship Analyses and Molecular Modeling. In this section, we examine the pharmacological data obtained for the newly synthesized series (Tables 2–6) and analyze the effect of halogenation in the structure–affinity (SAR) and structure–selectivity (SSR) relationships. All ligands were evaluated as racemic mixtures and comparative studies used as a reference of the parent series (Table 1). The SAR here outlined is then further assessed by FEP calculations in the context of a refined computational 3D model of $hA_{2B}AR$.

The adenosinergic affinity profiles of the 80 alkyl 7/8-halo-4-heteroaryl-1,4-dihydro-benzo[4,5]imidazo[1,2-*a*]pyrimidine-3-carboxylates are presented in Tables 2–6. Up to 25 ligands

https://doi.org/10.1021/acs.jmedchem.2c01768
J. Med. Chem. 2023, 66, 890–912

Table 2. Structure and Adenosine Receptor Affinities of Series I: Alkyl 7,8-Dihalo-1,4-dihydrobenzo[4,5]imidazo[1,2-*a*]pyrimidine-3-carboxylates (Cmpds 14a−x)

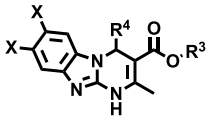

				K_i (nM) or % at 1 μM			
compound	R^4	R^3	X	hA_1 [a]	hA_{2A} [b]	hA_{2B} [c]	hA_3 [d]
14a	2-furyl	Et	F	1%	2%	44.1 ± 1.7	2%
14b	2-furyl	*i*-Pr	F	13%	22%	11.9 ± 1.1	14%
14c	3-furyl	Et	F	22%	36%	28.2 ± 0.8	17%
14d	3-furyl	*i*-Pr	F	17%	16%	52.9 ± 1.5	20%
14e	2-thienyl	Et	F	2%	3%	25%	5%
14f	2-thienyl	*i*-Pr	F	1%	1%	1%	10%
14g	3-thienyl	Et	F	1%	1%	519 ± 7	5%
14h	3-thienyl	*i*-Pr	F	1%	3%	43%	4%
14i	2-furyl	Et	Cl	2%	5%	9%	1%
14j	2-furyl	*i*-Pr	Cl	43%	12%	117 ± 5	7%
14k	3-furyl	Et	Cl	33%	34%	54.7 ± 3.2	6%
14l	3-furyl	*i*-Pr	Cl	4%	31%	36%	8%
14m	2-thienyl	Et	Cl	2%	1%	9%	11%
14n	2-thienyl	*i*-Pr	Cl	1%	4%	1%	9%
14o	3-thienyl	Et	Cl	5%	1%	9%	1%
14p	3-thienyl	*i*-Pr	Cl	2%	1%	359 ± 4	6%
14q	2-furyl	Et	Br	1%	17%	37%	2%
14r	2-furyl	*i*-Pr	Br	11%	28%	62.6 ± 1.9	21%
14s	3-furyl	Et	Br	2%	2%	7%	10%
14t	3-furyl	*i*-Pr	Br	1%	1%	32%	9%
14u	2-thienyl	Et	Br	2%	7%	12%	5%
14v	2-thienyl	*i*-Pr	Br	1%	1%	9%	3%
14w	3-thienyl	Et	Br	2%	7%	47%	4%
14x	3-thienyl	*i*-Pr	Br	4%	1%	9%	8%
DPCPX				2.20 ± 0.2	157 ± 3	73.2 ± 1.4	1722 ± 11
ZM241385				683 ± 4	1.9 ± 0.1	65.7 ± 1.1	863 ± 4
NECA				14.0 ± 1	20.0 ± 3	2400 ± 35	6.20 ± 0.9

[a]Displacement of specific [^{3}H]DPCPX binding in human CHO cells expressed as K_i in nanomolars (n = 3) or percentage displacement of specific binding at a concentration of 1 μM (n = 2). [b]Displacement of specific [^{3}H]4-(2-[7-amino-2-(2-furyl)[1,2,4]triazolo[2,3-*a*][1,3,5]triazin-5-ylamino]ethyl)phenol binding in human HeLa cells expressed as K_i in nanomolars (n = 3) or percentage displacement of specific binding at a concentration of 1 μM (n = 2). [c]Displacement of specific [^{3}H]DPCPX binding in human HEK-293 cells expressed as K_i in nanomolars (n = 3) or percentage displacement of specific binding at a concentration of 1 μM (n = 2). [d]Displacement of specific [^{3}H]NECA binding in human HeLa cells expressed as K_i in nanomolars (n = 3) or percentage displacement of specific binding at a concentration of 1 μM (n = 2).

combine attractive A_{2B}AR affinity (K_i <50 nM) and exquisite subtype selectivity (>1000-fold), from which 14 ligands exhibit outstanding A_{2B}AR affinity (K_i <10 nM) [e.g., compounds **16a**, **16b**, **16d**, **16i**, **16j**, **16k**, **16l**, **16r**, **16s**, **16t** (Table 4), **17b**, **18b**, **18c**, and **18d** (Table 5)]. The available data reveal interesting and previously unexplored SAR trends, with derivatives bearing a halogen atom at position 8 of the heterotricyclic core collectively emerging as the most appealing A_{2B}AR antagonists in these series (series **III** and **IV**, Tables 4 and 5). Compared to the congeners of the parent series (Table 1), 10 of the ligands here identified present improved pharmacodynamic and PK profiles, with ligands **16b**, **16j**, **16r**, and **16s** deserving particular attention, as they exhibit one-digit K_i values (3−5 nM) and excellent subtype selectivity, thus justifying the selection of these compounds for further intrinsic activity assays (see the previous section).

A comparative analysis of the binding data obtained for the parent series (Table 1) and ligands of series **I** (Table 2) evidenced that a simultaneous introduction of halogens at positions 7 and 8 has deleterious impact on A_{2B}AR affinity. Moreover, it can be observed that this reduction in affinity is halogen dependent, with better affinity profiles observed for some 7,8-difluoro derivatives (Table 2, Cmpds **14a−d**) and the affinity decay being proportional to the atomic radius of the halogen (Table 2 and Supplementary Figure S3). Ligands bearing a thienyl ring at position 4 of the heterotricyclic scaffold are inactive with the only exception of the low-affinity **14p**. For the case of ligands containing a furyl group at R^4, the A_{2B}AR affinity seems to be highly dependent of the halogens present (Table 2). Thus, all ligands containing a furyl group of the 7,8-difluorinated scaffold (Cmpds **14a−d**) elicit potent A_{2B}AR affinity (K_i = 11.9−52.9 nM) irrespective of the substitution pattern at the furan ring (2-furyl or 3-furyl) or the alkoxy residue in the ester moiety (R^3). Although potent, the difluorinated derivatives **14a−d** show lower affinity (threefold) than their parent series analogues (Table 1). Similarly, in the subsets bearing chlorine atoms (Table 2, Cmpds **14i−p**), only the derivatives incorporating an optimal substituent at R^4 and R^3 (**14j** and **14k**) show moderate affinity. Following this trend, the only derivative retaining A_{2B}AR affinity in the 7,8-dibromo

https://doi.org/10.1021/acs.jmedchem.2c01768
J. Med. Chem. 2023, 66, 890−912

Table 3. Structure and Adenosine Receptor Affinities of Series II: Alkyl 7-Halo-1,4-dihydrobenzo[4,5]imidazo[1,2-*a*]pyrimidine-3-carboxylates (Cmpds 15a−x)

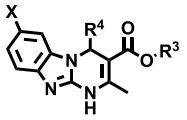

				K_i (nM) or % at 1 μM			
compound	R^4	R^3	X	hA_1[a]	hA_{2A}[b]	hA_{2B}[c]	hA_3[d]
15a	2-furyl	Et	F	16%	2%	67.5 ± 3.1	10%
15b	2-furyl	*i*-Pr	F	32%	3%	12.2 ± 1.2	5%
15c	3-furyl	Et	F	26%	21%	25.0 ± 1.5	5%
15d	3-furyl	*i*-Pr	F	25%	11%	136 ± 7	6%
15e	2-thienyl	Et	F	25%	1%	37%	11%
15f	2-thienyl	*i*-Pr	F	11%	2%	23%	6%
15g	3-thienyl	Et	F	7%	1%	1031 ± 95	3%
15h	3-thienyl	*i*-Pr	F	1%	1%	764 ± 11	1%
15i	2-furyl	Et	Cl	26%	2%	18%	4%
15j	2-furyl	*i*-Pr	Cl	667 ± 12	17%	44.3 ± 1.4	5%
15k	3-furyl	Et	Cl	22%	30%	47.3 ± 1.9	3%
15l	3-furyl	*i*-Pr	Cl	6%	4%	50%	3%
15m	2-thienyl	Et	Cl	2%	3%	1%	1%
15n	2-thienyl	*i*-Pr	Cl	1%	3%	7%	1%
15o	3-thienyl	Et	Cl	4%	2%	50%	3%
15p	3-thienyl	*i*-Pr	Cl	7%	9%	48%	3%
15q	2-furyl	Et	Br	22%	21%	48%	5%
15r	2-furyl	*i*-Pr	Br	46%	1%	273 ± 4	6%
15s	3-furyl	Et	Br	10%	1%	318 ± 6	19%
15t	3-furyl	*i*-Pr	Br	11%	3%	26%	12%
15u	2-thienyl	Et	Br	1%	5%	1%	4%
15v	2-thienyl	*i*-Pr	Br	1%	6%	11%	8%
15w	3-thienyl	Et	Br	4%	3%	43%	3%
15x	3-thienyl	*i*-Pr	Br	1%	1%	10%	1%
DPCPX				2.20 ± 0.2	157 ± 3	73.2 ± 1.4	1722 ± 11
ZM241385				683 ± 4	1.9 ± 0.1	65.7 ± 1.1	863 ± 4
NECA				14.0 ± 1	20.0 ± 3	2400 ± 35	6.20 ± 0.9

[a]Displacement of specific [^{3}H]DPCPX binding in human CHO cells expressed as K_i in nanomolars (n = 3) or percentage displacement of specific binding at a concentration of 1 μM (n = 2). [b]Displacement of specific [^{3}H]4-(2-[7-amino-2-(2-furyl)[1,2,4]triazolo[2,3-*a*][1,3,5]triazin-5-ylamino]ethyl)phenol binding in human HeLa cells expressed as K_i in nM (n = 3) or percentage displacement of specific binding at a concentration of 1 μM (n = 2). [c]Displacement of specific [^{3}H]DPCPX binding in human HEK-293 cells expressed as K_i in nanomolars (n = 3) or percentage displacement of specific binding at a concentration of 1 μM (n = 2). [d]Displacement of specific [^{3}H]NECA binding in human HeLa cells expressed as K_i in nanomolars (n = 3) or percentage displacement of specific binding at a concentration of 1 μM (n = 2).

subset is **14r** (K_i = 62.6 nM), containing at R^4 and R^3 the same substitution pattern of the lead compound **ISAM-140**, albeit with a 20-fold decrease in affinity.

The adenosinergic profile obtained for series **II** is presented in Table 3. Here, introduction of a halogen at position 7 reproduced some of the SAR trends detected in series **I** (Table 2). While some attractive ligands can be identified (e.g., **15b** and **15c**, K_i = 12.2 and 25.0 nM, respectively), a comparison with the parent series (Table 1) revealed that halogenation at position 7 is deleterious. As for series **I**, the effect of halogenation relied on the nature of the halogen, with fluor being the best tolerated (Table 3, Cmpds **15a−d**). Similarly, most derivatives bearing thienyl groups remain inactive. For series bearing chloro and bromo atoms at position 7, only optimal pair combinations at R^4 and R^3 (e.g., 2-furyl and isopropyl, 3-furyl and ethyl, respectively) produced ligands with moderate (K_i ∼ 45 nM) affinity (Table 3, Cmpds **15j**, **15k**, **15r**, and **15s**). This trend is also observed for 7-fluoro derivatives (Table 3, Cmpds **15a−15d**), while in this subset, all furyl-containing derivatives exhibited attractive A_{2B}AR affinity (K_i = 12.2−136 nM).

An evaluation of series **III** (Table 4) enabled the identification of the most potent (K_i < 10 nM) A_{2B}AR antagonists described in this study. It also allowed to envision the significant effect of halogen substitution at position 8 and its rationalization from a molecular modeling perspective. In contrast to previous series, halogenation at position 8 systematically improved the A_{2B}AR affinity irrespective of the nature of the halogen atom (Table 4 and Figure 5). Indeed, most 8-halo derivatives have measurable A_{2B}AR affinity values (Table 4). All 8-halogenated derivatives bearing a furan ring at position 4 exhibit excellent A_{2B}AR affinity (K_i = 3.05−26.9 nM), indeed generally superior by 4−10-fold to their analogues in the parent series (Figure 5). A similar trend, but with attenuated affinity, is observed for thiophene-based analogues (K_i = 61.1−911 nM). It should also be noticed that for thienyl derivatives, the introduction of a halogen at position 8 does not improve A_{2B}AR affinities as compared to the non-halogenated parent compounds (Table 1). A direct compar-

https://doi.org/10.1021/acs.jmedchem.2c01768
J. Med. Chem. 2023, 66, 890−912

Table 4. Structure and Adenosine Receptor Affinities of Series III: Alkyl 8-Halo-1,4-dihydrobenzo[4,5]imidazo[1,2-*a*]pyrimidine-3-carboxylates (Cmpds 16a−x)

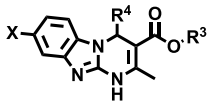

compound	R^4	R^3	X	K_i (nM) or % at 1 μM			
				hA_1[a]	hA_{2A}[b]	hA_{2B}[c]	hA_3[d]
16a	2-furyl	Et	F	10%	29%	6.60 ± 1.0	2%
16b (ISAM-163)	2-furyl	*i*-Pr	F	11%	2%	3.05 ± 0.7	3%
16c	3-furyl	Et	F	29%	21%	13.7 ± 0.9	2%
16d	3-furyl	*i*-Pr	F	14%	31%	8.60 ± 0.5	4%
16e	2-thienyl	Et	F	1%	3%	724 ± 8	3%
16f	2-thienyl	*i*-Pr	F	2%	1%	668 ± 6	7%
16g	3-thienyl	Et	F	1%	1%	187 ± 2	3%
16h	3-thienyl	*i*-Pr	F	2%	1%	75.5 ± 3.2	5%
16i	2-furyl	Et	Cl	23%	10%	8.42 ± 1.4	4%
16j (ISAM-161)	2-furyl	*i*-Pr	Cl	35%	24%	5.03 ± 0.3	2%
16k	3-furyl	Et	Cl	31%	43%	7.21 ± 0.4	4%
16l (ISAM-M89A)	3-furyl	*i*-Pr	Cl	27%	176 ± 4	6.10 ± 0.7	1%
16m	2-thienyl	Et	Cl	3%	2%	41%	1%
16n	2-thienyl	*i*-Pr	Cl	2%	2%	837 ± 11	1%
16o	3-thienyl	Et	Cl	2%	7%	911 ± 14	8%
16p	3-thienyl	*i*-Pr	Cl	7%	7%	165 ± 9	4%
16q	2-furyl	Et	Br	18%	29%	26.9 ± 0.8	33%
16r (ISAM-157)	2-furyl	*i*-Pr	Br	25%	2%	5.23 ± 0.4	10%
16s (ISAM-M114A)	3-furyl	Et	Br	1%	37%	3.32 ± 0.4	25%
16t	3-furyl	*i*-Pr	Br	2%	509 ± 6	8.20 ± 1.1	2%
16u	2-thienyl	Et	Br	6%	3%	55%	6%
16v	2-thienyl	*i*-Pr	Br	1%	1%	115 ± 3	1%
16w	3-thienyl	Et	Br	1%	9%	537 ± 8	1%
16x	3-thienyl	*i*-Pr	Br	2%	1%	61.1 ± 1.8	4%
DPCPX				2.20 ± 0.2	157 ± 3	73.2 ± 1.4	1722 ± 11
ZM241385				683 ± 4	1.9 ± 0.1	65.7 ± 1.1	863 ± 4
NECA				14.0 ± 1	20.0 ± 3	2400 ± 35	6.20 ± 0.9

[a]Displacement of specific [^{3}H]DPCPX binding in human CHO cells expressed as K_i in nanomolars (n = 3) or percentage displacement of specific binding at a concentration of 1 μM (n = 2). [b]Displacement of specific [^{3}H]4-(2-[7-amino-2-(2-furyl)[1,2,4]triazolo[2,3-*a*][1,3,5]triazin-5-ylamino]ethyl)phenol binding in human HeLa cells expressed as K_i in nanomolars (n = 3) or percentage displacement of specific binding at a concentration of 1 μM (n = 2). [c]Displacement of specific [^{3}H]DPCPX binding in human HEK-293 cells expressed as K_i in nanomolars (n = 3) or percentage displacement of specific binding at a concentration of 1 μM (n = 2). [d]Displacement of specific [^{3}H]NECA binding in human HeLa cells expressed as K_i in nanomolars (n = 3) or percentage displacement of specific binding at a concentration of 1 μM (n = 2).

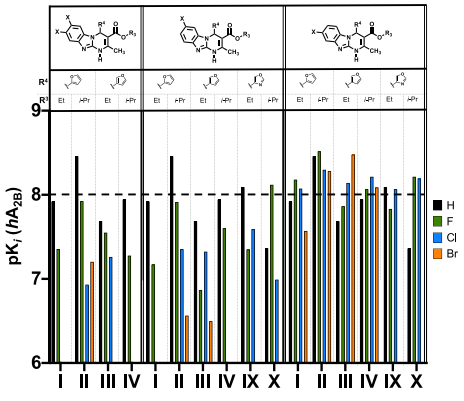

Figure 5. Interleaved bar chart showing A_{2B}AR pK_i [−log(K_i)] for the halogenation of furyl and oxazolyl scaffolds (represented at the *x*-axis as **I**−**IV** and **IX**−**X**). Black: non-halogenated, green: fluorinated, cyan: chlorinated, and orange: brominated compounds.

ison of the A_{2B}AR affinity profile (pK_i) of selected derivatives of different series is presented in Figure 5.

The pharmacological data obtained for the exploratory derivatives bearing a 4-oxazolyl residue at position 4 of the tricyclic core (series **IV**, Table 5) introduced new SAR perspectives. Although in general this series reproduced the most prominent SAR trends discussed for the previous series, the effect of halogenation seems to be less marked if compared to their parent compounds (Table 1>, Cmpds **IX** and **X**). Collectively, 8-halo derivatives in this series (Table 5, Cmpds **18a−18d**) exhibit excellent A_{2B}AR affinity (K_i 6.10−14.7 nM). A comparative analysis reveals that the affinity data in this series is lightly superior to the 7-halo analogues (Table 5, Cmpds **17a−17d**) or the parent compounds in the prototype series (Table 1, Cmpds **IX** and **X**). These data highlight the interest of the 4-oxazolyl moiety as a privileged non-furane core at A_{2B}AR, which, in addition to a superior metabolic stability profile, can capture the two productive interactions predicted for 2-furyl and 3-furyl rings within the A_{2B}AR orthosteric binding site. This allows for better accommodation of the compounds at A_{2B}AR (Supplementary Figure S4), even allowing a successful fitting of the 7-halo derivatives (Table 5).

https://doi.org/10.1021/acs.jmedchem.2c01768
J. Med. Chem. 2023, 66, 890−912

Table 5. Structure and Adenosine Receptor Affinities of Series IV: Alkyl 7/8-Halo 4-(oxazol-4-yl)-1,4-dihydrobenzo[4,5]imidazo[1,2-*a*]pyrimidine-3-carboxylates (Cmpds 17a−d and 18a−d)

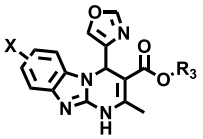

			K_i (nM) or % at 1 μM			
compound	R^3	X	hA_1[a]	hA_{2A}[b]	hA_{2B}[c]	hA_3[d]
17a	Et	7-F	43%	4%	44.7 ± 1.4	26%
17b (ISAM-R324B)	*i*-Pr	7-F	34%	19%	7.60 ± 0.6	22%
17c	Et	7-Cl	227 nM	14%	25.6 ± 1.2	11%
17d	*i*-Pr	7-Cl	27%	1%	102 ± 7	20%
18a	Et	8-F	25%	16%	14.7 ± 1.1	16%
18b (ISAM-R324A)	*i*-Pr	8-F	29%	20%	6.10 ± 0.3	20%
18c (ISAM-R316A)	Et	8-Cl	30%	13%	8.60 ± 0.4	15%
18d (ISAM-R319A)	*i*-Pr	8-Cl	23%	35%	6.40 ± 0.7	23%
DPCPX			2.20 ± 0.2	157 ± 3	73.2 ± 1.4	1722 ± 11
ZM241385			683 ± 4	1.9 ± 0.1	65.7 ± 1.1	863 ± 4
NECA			14.0 ± 1	20.0 ± 3	2400 ± 35	6.20 ± 0.9

[a]Displacement of specific [^{3}H]DPCPX binding in human CHO cells expressed as K_i in nanomolars (n = 3) or percentage displacement of specific binding at a concentration of 1 μM (n = 2). [b]Displacement of specific [^{3}H]4-(2-[7-amino-2-(2-furyl)[1,2,4]triazolo[2,3-*a*][1,3,5]triazin-5-ylamino]ethyl)phenol binding in human HeLa cells expressed as K_i in nanomolars (n = 3) or percentage displacement of specific binding at a concentration of 1 μM (n = 2). [c]Displacement of specific [^{3}H]DPCPX binding in human HEK-293 cells expressed as K_i in nanomolars (n = 3) or percentage displacement of specific binding at a concentration of 1 μM (n = 2). [d]Displacement of specific [^{3}H]NECA binding in human HeLa cells expressed as K_i in nanomolars (n = 3) or percentage displacement of specific binding at a concentration of 1 μM (n = 2).

Due to their dual A_{2A}/A_{2B}AR profile, two ligands (Table 4, Cmpds **16l** and **16t**) caught our interest during the analysis of SAR trends within the series of 8-halo derivatives. Both ligands combine the excellent A_{2B}AR affinity of this subset (K_i = 6.10 and 8.20 nM, respectively), with an incipient affinity by A_{2A}AR (K_i = 176 and 509 nM, respectively). While sharing a common structural pattern (e.g., a 3-furyl ring at R^4 and isopropyl group in the alkoxy residue of the ester function at R^3), they differ in the halogen atom at position 8 (Cl vs Br). Despite being equipotent at A_{2B}AR, the important differences in A_{2A}AR affinity (threefold) suggest that the chlorine atom is better tolerated for the binding at A_{2A}AR. With further studies currently in progress to explore in depth the structural requirements for dual A_{2A}AR/A_{2B}AR antagonism, substitution at position 8 appears to be a key structural requirement for dual blockade of both receptors. It should be noticed that the dual A_{2A}AR/A_{2B}AR profile of **16l** is interesting in the context of cancer (immuno)therapy, with two compounds showing similar profiles in clinical trials.[44] Indeed, this dual profile allowed us to include compound **16l** in a recent study with ex vivo assays to study the potential of the A_{2B}AR antagonism in the context of cancer immunotherapy.[36]

Enantiospecific Binding to A_{2B}AR. The four series of A_{2B}AR antagonists herein documented were initially obtained and tested as racemates (Tables 2−5). The stereocenter within the heterocyclic core is a signature element of our ligands,[25,31,33−35] which plays an important role for the recognition within the A_{2B}AR binding pocket, providing structural singularity with respect to known planar A_{2B}AR ligands (e.g., xanthines). Early molecular models and FEP calculations, supported by experimental data, predicted that only one enantiomer should bind to the orthosteric site of A_{2B}AR. To further elucidate the molecular basis underlying enantioselective recognition in these series and to expand the repertoire of stereoselective A_{2B}AR antagonists, we proceeded with enantiomeric separation, assignment, and biological evaluation (Table 6) of a representative subset of A_{2B}AR antagonists. A validated approach using chiral HPLC, circular dichroism (CD) spectroscopy, and X-ray crystallography (Figure 6)[25,31,33−35] was employed to separate and assign the configuration of six representative A_{2B}AR antagonists [(±)-**16b**, (±)-**16j**, (±)-**16l**, (±)-**16r**, (±)-**16s**, and (±)-**18c**] and the prototype ligand of the parent series [(±) **ISAM-140**]. Semipreparative HPLC separation of the selected racemic ligands on a chiral stationary phase (Figure 6 and Experimental section) afforded each enantiomer with excellent stereochemical purity (i.e., >97%). As documented for different Biginelli-based scaffolds,[45] the sign of the distinctive CD activity of the enamide group (around 300 nm) allows the unequivocal assignment of the absolute configuration of each enantiomer (Figure 7). At that wavelength, enantiomers showing a negative Cotton effect (intense line) contain the pentagonal heterocycle (furan or oxazole) backward while the stereoisomers giving a positive Cotton effect (clear line) contain the heterocyclic core forward. As a complement of these studies, a structural analysis of monocrystals of (*S*)-**16s** and (*R*)-**16s**, through X-ray crystallography (Figure 6A,B), provided additional experimental evidence corroborating the CD-assisted stereochemical configuration (Figure 7).

The affinity profile of the obtained enantiomers at the four human ARs, together with the corresponding racemic ligands, is shown in Table 6. Inspection of the obtained data confirm that the observed A_{2B}AR affinity within the racemic ligands is exclusively due to one of the stereoisomers, in line with the A_{2B}AR enantiospecific recognition model documented for structurally analogous series.[25,31,33,34] In all cases, the eutomers (which contain the pentagonal core backward) are nearly twofold more potent than their corresponding racemate, whereas the other stereoisomer is devoid in all cases of any affinity at the four ARs (Table 6 and Figure 7). Particularly

https://doi.org/10.1021/acs.jmedchem.2c01768
J. Med. Chem. 2023, 66, 890−912

Table 6. Structure and Adenosine Receptor Affinities of Racemic and Enantiomers of Selected Ligands

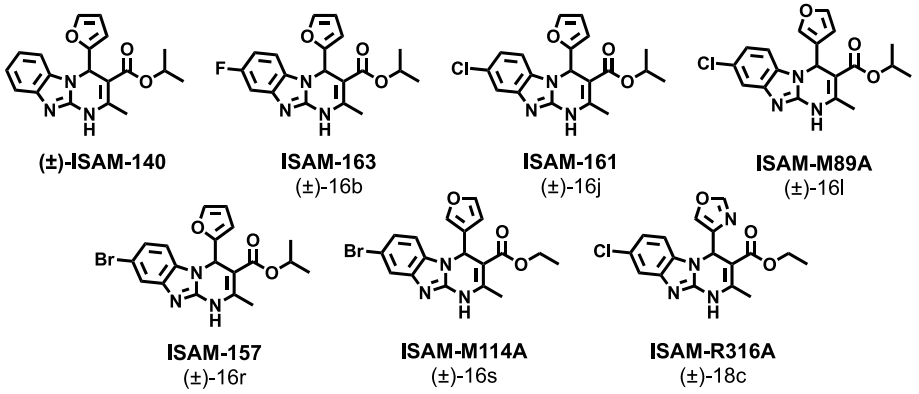

compound	R^4	R^3	R^8	K_i (nM) or % at 1 μM			
				hA_1[a]	hA_{2A}[b]	hA_{2B}[c]	hA_3[d]
(±)-ISAM-140	2-furyl	*i*-Pr	H	20%	28%	3.49 ± 0.2	2%
ISAM-140	2-furyl	*i*-Pr	H	14%	7%	17%	3%
(*S*)-ISAM-140	2-furyl	*i*-Pr	H	2%	12%	0.89 ± 0.2	4%
(±)-16b [(±)-ISAM-163]	2-furyl	*i*-Pr	F	21%	2%	3.05 ± 0.7	3%
(*R*)-16b(*R*)-ISAM-163]	2-furyl	*i*-Pr	F	15%	5%	41%	19%
(*S*)-16b [(*S*)-ISAM-163]	2-furyl	*i*-Pr	F	26%	11%	0.94 ± 0.1	12%
(±)-16j [(±)-ISAM-161]	2-furyl	*i*-Pr	Cl	35%	24%	5.03 ± 0.3	2%
(*R*)-16j [(*R*)-ISAM-161]	2-furyl	*i*-Pr	Cl	7%	37%	51%	5%
(*S*)-16j [(*S*)-ISAM-161]	2-furyl	*i*-Pr	Cl	48%	19%	2.04 ± 0.2	6%
(±)-16l [(±)-ISAM-M89A]	3-furyl	*i*-Pr	Cl	27%	176 ± 4	6.10 ± 0.7	1%
(*S*)-16l [(*S*)-ISAM-M89A]	3-furyl	*i*-Pr	Cl	24%	25%	53%	19%
(*R*)-16l [(*R*)-ISAM-M89A]	3-furyl	*i*-Pr	Cl	37%	96.3 ± 6	2.6 ± 0.3	24%
(±)-16r [(±)-ISAM-157]	2-furyl	*i*-Pr	Br	25%	2%	5.23 ± 0.4	10%
(*R*)-16r [(*R*)-ISAM-157]	2-furyl	*i*-Pr	Br	12%	7%	35%	2%
(*S*)-16r [(*S*)-ISAM-157]	2-furyl	*i*-Pr	Br	32%	14%	2.97 ± 0.4	6%
(±)-16s [(±)-ISAM-M114A]	3-furyl	Et	Br	1%	37%	3.32 ± 0.4	25%
(*R*)-16s [(*R*)-ISAM-M114A]	3-furyl	Et	Br	10%	12%	1.17 ± 0.1	14%
(*S*)-16s [(*S*)-ISAM-M114A]	3-furyl	Et	Br	11%	16%	34%	10%
(±)-18c [(±)-ISAM-R316A]	4-oxazolyl	Et	Cl	30%	13%	8.60 ± 0.4	15%
(*R*)-18c [(*R*)-ISAM-R316A]	4-oxazolyl	Et	Cl	9%	32%	26%	15%
(*S*)-18c [(*S*)-ISAM-R316A]	4-oxazolyl	Et	Cl	22%	17%	3.39 ± 0.2	6%
DPCPX				2.20 ± 0.2	157 ± 3	73.2 ± 1.4	1722 ± 11
ZM241385				683 ± 4	1.9 ± 0.1	65.7 ± 1.1	863 ± 4
NECA				14.0 ± 1	20.0 ± 3	2400 ± 35	6.20 ± 9

[a]Displacement of specific [^{3}H]DPCPX binding in human CHO cells expressed as K_i in nanomolars (n = 3) or percentage displacement of specific binding at a concentration of 1 μM (n = 2). [b]Displacement of specific [^{3}H]4-(2-[7-amino-2-(2-furyl)[1,2,4]triazolo[2,3-*a*][1,3,5]triazin-5-ylamino]ethyl)phenol binding in human HeLa cells expressed as K_i in nanomolars (n = 3) or percentage displacement of specific binding at a concentration of 1 μM (n = 2). [c]Displacement of specific [^{3}H]DPCPX binding in human HEK-293 cells expressed as K_i in nanomolars (n = 3) or percentage displacement of specific binding at a concentration of 1 μM (n = 2). [d]Displacement of specific [^{3}H]NECA binding in human HeLa cells expressed as K_i in nanomolars (n = 3) or percentage displacement of specific binding at a concentration of 1 μM (n = 2).

noticeable are the two eutomers [(*S*)-**16b** and (*S*)-**ISAM-140**] with sub-nanomolar A_{2B}AR affinities. The eutomer (*R*)-**16l**, containing the pentagonal core backward (Figure 6C), emerges as the first example of a dual A_{2A}/A_{2B}AR ligand exhibiting enantiospecific recognition at both receptors, since its enantiomer (which contain the pentagonal core forward, Figure 6D) is completely inactive. The enantioselective recognition reported here for (*R*)-**16l** has inspired the design of a new series of non-planar dual antagonists that will be reported on due time.

To provide a further structural rationale, we calculated the relative binding free energy difference between each pair of enantiomers for compounds **ISAM-140**, **16b**, **16j**, **16l**, and **18c** (Figure 8A). The corresponding FEP simulations were run taking as starting point the binding model proposed earlier for this scaffold,[25] illustrated in Figure 6C,D. The binding mode of the eutomers (Figure 6C) has been largely explored with FEP simulations on previous series, allowing a rationalization of the observed SAR.[31,33] In the present computational analysis, we assumed an analogous binding orientation for the distomer (Figure 6D), although there can be other possibilities, which is difficult to assess given the inactive profile of these enantiomers. Nevertheless, the qualitative agreement with the experimental profile is remarkable, as the simulations indicate a clear binding preference for the eutomer in all five cases (Figure 8A). These data confirm our previous computational models for enantiospecific recognition of structurally related Biginelli-based scaffolds,[46] which was used to assess the growth of these scaffolds.

https://doi.org/10.1021/acs.jmedchem.2c01768
J. Med. Chem. 2023, 66, 890−912

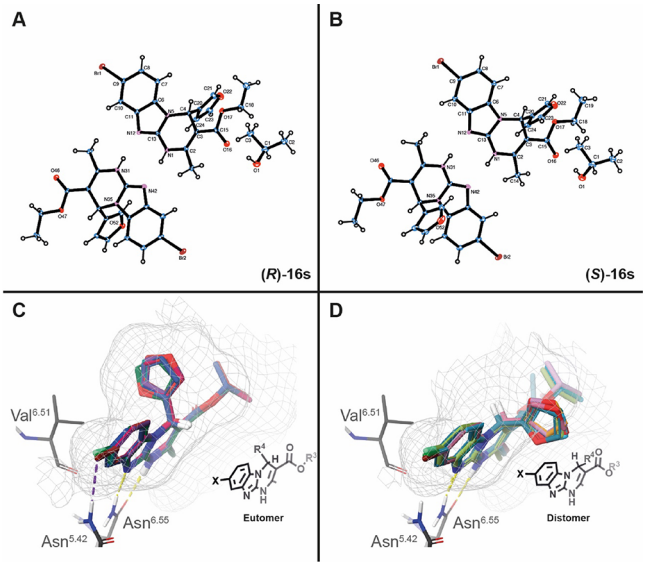

Figure 6. (A) X-ray crystal structure of (*R*)-**16s** (CCDC: 2048281). (B) (*S*)-**16s** (CCDC: 2047365). (C) Docking superposition for eutomers (*S*)-**ISAM-140**, (*S*)-**16b**, (*S*)-**16j**, (*R*)-**16l**, (*S*)-**16r**, (*R*)-**16s**, and (*S*)-**18c** (A_{2B}AR homology model from A_{2A}AR, PDB: 3EML). Highlight the formation of a halogen bridge with 8-chlorine and 8-bromine compounds ($Asn^{5.42}$). (D) Docking superposition for distomers (*R*)-**ISAM-140**, (*R*)-**16b**, (*R*)-**16j**, (*S*)-**1i** (*R*)-**16r**, (*S*)-**16s**, and (*R*)-**18c** (A_{2B}AR homology model from A_{2A}AR, PDB: 3EML). Gray mesh represents the A_{2B}AR binding site surface.

Docking and FEP Simulations on the Eutomers. Using the stereospecific binding mode established in the previous stage, we set up a systematic scheme of FEP simulations aimed to provide structural understanding to the observed SAR. To this end, we selected all 56 compounds with measured experimental affinity for hA_{2B}AR (K_i (<1000 nM) and ran a series of alchemical transformations to obtain relative binding free energies (RBFE), by FEP transformation of the substituents on positions 7 and 8, while retaining the same substituents on R^3 and R^4. Within each congeneric series (as defined in Table 1 for reference compounds), the compound pairs for the FEP simulations were defined by our mapping algorithm, and the absolute binding free energies (ABFE) were estimated following a cycle closure correction, taking the experimental affinity value of one compound as a reference (see Supplementary Table S3). With this approach, we maintained simplicity within the alchemical transformations, ensuring a good convergence (average SEM = 0.44 kcal/mol). The pulled results obtained for all congeneric series are summarized in Figure 8C and Supplementary Figure S5. The correlation between calculated and experimental binding free energies is very good, according to the low value for the mean unassigned error (MUE = 1.08 kcal/mol). A closer look into the data revealed that most of this unassigned error is caused by the group of brominated compounds (red symbols, Figure 8B), which show a tendency to overprediction. The binding model proposed is thus reinforced by these calculations, which correctly reproduce the global SAR outlined in the previous section. Experimentally, we observed that 7-halogenated substitutions show halogen size-dependent A_{2B}AR affinity. The pattern observed for the 7,8-dihalogenated compounds seems to confirm this tendency, while 8-halogenated compounds show a halogen-size-independent A_{2B}AR affinity (Figure 9). According to our binding model, the bulkier Cl and Br substituents on the last position can make a halogen-bond interaction with $Asn^{5.42}$, counterbalancing the excess of volume on position 8, something that is not possible when the halogen is on position 7, resulting in a decrease in affinity proportional to the volume of the buried halogen atom (Supplementary Figure S4).

Preliminary ADMET Exploration. An early understanding of the ADMET (absorption, distribution, metabolism, excretion, and toxicity) profile of prototypical new lead compounds is crucial to reducing attrition and accelerating upstream drug discovery programs.[47,48] As reported in the bibliography, halogenation, and particularly fluorination, usually enhances the metabolic stability of chemical scaffolds.[49,50] To preliminarily explore the in vitro ADMET profile of the series documented here, seven representative A_{2B}AR antagonists (**14b**, **15j**, **16b**, **16j**, **16l**, **16r**, and **18b**) were selected to evaluate their solubility, liver microsome stability, and inhibitory profile toward a prototypic cytochrome enzyme (CYP3A4). The selected compounds allow not only a preliminary evaluation of the impact of mono- or di-halogenation (positions 7, 8, or 7,8) but also to analyze the effect of different atoms (F, Cl, Br) on the PK parameters evaluated, while the inclusion of ligand **18b** allowed us to assess the effect of fluorination on a representative non-furan A_{2B}AR antagonist. Table 8 shows the PK data obtained for the selected compounds; for comparison, the PK data available for the non-halogenated reference compounds (Cmpds **II** and **X**) is included in Table 8, together with the adenosinergic data ($hA_{2B}K_i$ in nanomolars, and $hA_{2A}K_i$ for **16l**) in order to facilitate an integrated analysis for these compounds.

All ligands evaluated exhibit excellent solubility (21−70 μM) in PBS at pH 7, especially if compared to the solubility reported for a potent xanthine-based antagonist (PSB-603, Table 8).[28] The introduction of fluorine atoms (7,8-difluoro, 7-fluoro, and 8-fluoro) improves up to twofold the solubility measured for the non-halogenated parent compounds. This trend also holds for the compound bearing an oxazole ring at position 4 (**18b**). Chlorination at position 8 does not improve or slightly decreases solubility (see data for **16j** and **16l**), whereas bromination greatly increases solubility [e.g., **16r** (70.7 μM) vs **ISAM-140** (25.2 μM)]. Liver microsome assay data (Table 8) revealed that the selected A_{2B}AR antagonists showed moderate stability, with 16−41% of the compound remaining after 60 min of exposure to human microsomes and half-life ranging from 21 to 45 min. These data suggest that microsomal stability directly correlates with halogen size [e.g., **16b** (F), **16j** (Cl), and **16r** (Br) with 19.83, 22.75, and 32.13% remanent at 60 min, respectively]. These findings are currently guiding an ongoing study to improve the microsomal stability of these promising A_{2B}AR antagonists.

To identify potential metabolic liabilities within the series here documented, the selected A_{2B}AR antagonists were tested in vitro for CYP3A4 inhibitory activity. CYP3A isoforms are ubiquitous in the liver, have a broad substrate specificity,[48] and are essential for the clearance of xenobiotics in humans (e.g., being involved in the metabolization of more than 50% of prescribed drugs). All experiments were performed in duplicate using fluorescence detection, employing ketoconazole as a reference compound (Table 8). The results of this study reveal IC_{50} values lower than 10 μM for all fluorinated compounds toward CYP3A4 (with inhibitory activity ranging from 31 to 40% at 10 μM), improving in all cases the measured CYP3A4 activity as compared to their non-halogenated congeners. A

https://doi.org/10.1021/acs.jmedchem.2c01768
J. Med. Chem. 2023, 66, 890−912

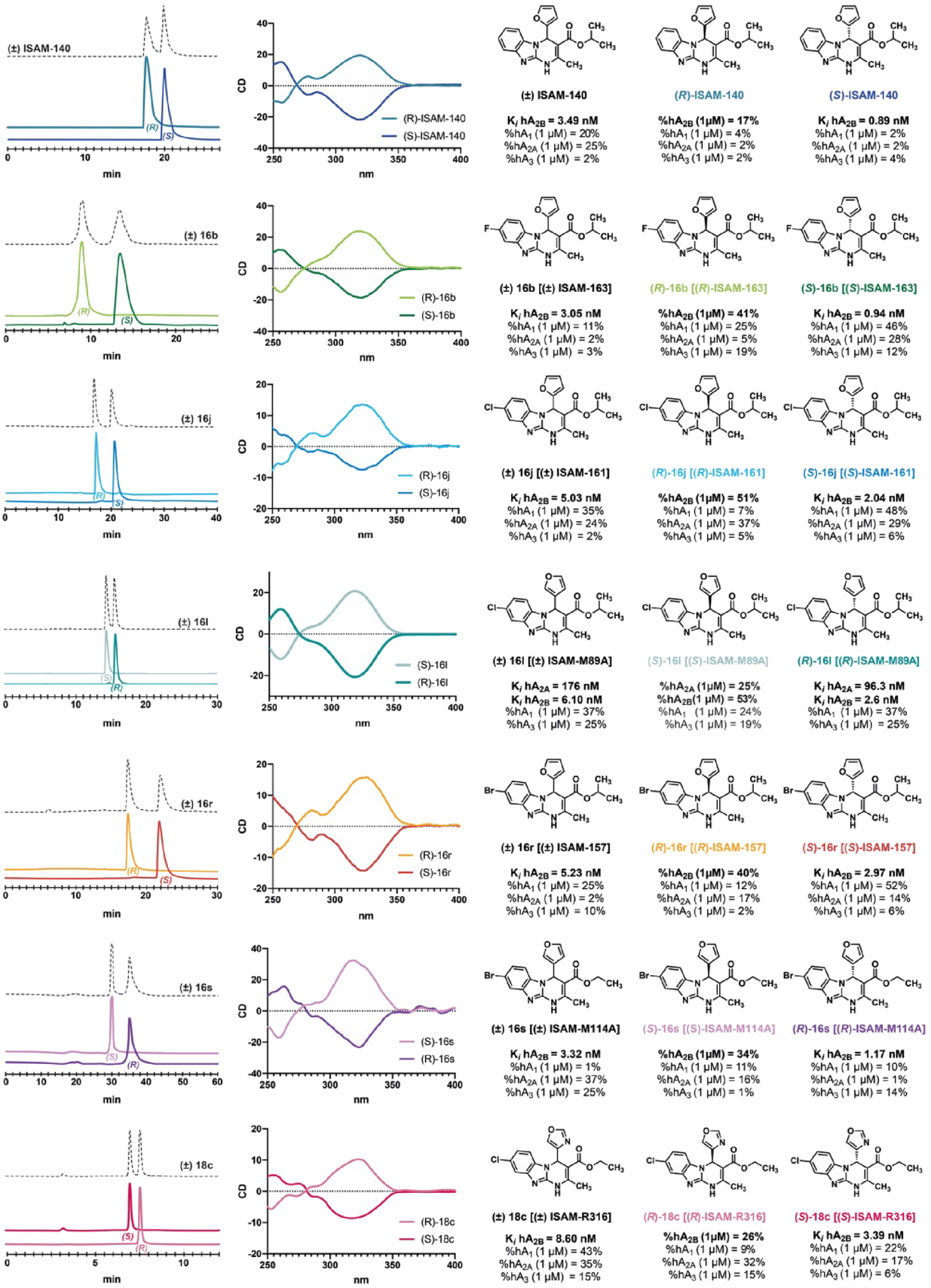

Figure 7. Chiral HPLC traces, circular dichroism spectra, and binding data of selected racemic ligands (**ISAM-140**, **16b**, **16j**, **16l**, **16r**, **16s**, and **18c**) and its enantiomers.

https://doi.org/10.1021/acs.jmedchem.2c01768
J. Med. Chem. 2023, 66, 890−912

Table 7. Functional Data of Compounds 16b, 16j, 16r, and 16s

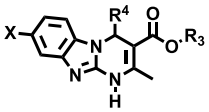

compound	R^4	R^3	X	K_i (hA_{2B})	K_B (hA_{2B})
(±)-16b (ISAM-163)	2-furyl	*i*-Pr	F	3.05 ± 0.7	0.80 ± 0.2
(±)-16j (ISAM-161)	2-furyl	*i*-Pr	Cl	5.03 ± 0.3	0.60 ± 0.2
(±)-16r (ISAM-157)	2-furyl	*i*-Pr	Br	5.23 ± 0.4	1.70 ± 0.6
(±)-16s (ISAM-M114A)	3-furyl	Et	Br	3.32 ± 0.4	1.50 ± 0.5

comparative analysis suggests that for 7-halo derivatives (Table 8, Cmpds **16b**, **16j**, and **16r**), increasing the size of the halogen increases the interaction with CYP3A4 (Table 8). Although the preliminary CYP3A4 data for three ligands seem to be suboptimal, we should keep in mind that the differences between the $hA_{2B}AR$ K_i of all compounds and the CYP3A4 IC_{50} (more than 200-fold in the worst case) makes CYP3A4 blockade not substantially important at the expected therapeutic doses. A more systematic study (e.g., including other relevant CYP subfamilies) would be required to draw definitive conclusions. In summary, an integrated analysis of pharmacodynamic studies and ADMET data allowed the identification of several new halogenated $A_{2B}AR$ antagonists that combine excellent affinity and selectivity and improved the ADMET profile.

In Vitro Evaluation of the Immunostimulatory Effect. Ado has proved to be a potent immunosuppressive metabolite that suppresses the functions of multiple types of immune cells. To gain evidence supporting the role of the here optimized $A_{2B}AR$ antagonists in the context of cancer immunotherapy, it was decided to evaluate the effect of two representative compounds (**16b** and **16j**) in the proliferative activity of a prototypical immune cell. The human peripheral blood mononuclear cells (PBMCs) were selected for the study; they are critical components of the immune system and are involved in both humoral and cell-mediated immunity. Ado-mediated blockade of PBMC proliferation is well documented and characterized;[51,52] we therefore investigated whether our $A_{2B}AR$ antagonists (**16b** and **16j**) can reverse the blockade of ADO-mediated proliferation in human PBMCs. PBMCs, isolated from a healthy donor, were labeled with carboxyfluorescein succinimidyl ester (CFSE) and then activated by adding anti-CD3/CD28 antibodies and interleukin 2 (IL-2). CFSE is a cell dye that allows for the determination of cell proliferation, as dividing cells progressively lose fluorescence. We found that, as expected, the addition of Ado caused a reduction in the frequency of PBMCs dividing cells (Figure 10A) and a corresponding increase of CFSE median fluorescence intensity (MFI) (Figure 10B) compared to the stimulated PBMCs. Notably, compounds **16b** and **16j** unequivocally reversed the Ado-induced blocking effect, resulting in an enhancement in the frequency of proliferative cells (Figure 10A,C−F) that correlates with a marked decrease in CFSE MFI (Figure 10B). From a quantitative point of view, the effect measured for compound **16b** (9.14%) is superior to that observed for **16j** (6.54%) (Figure 10D,E). Control experiments verified that the vehicle used to dissolve the compounds (DMSO) has a similar profile to that shown by ADO, thereby demonstrating that it does not favor PBMC proliferation by itself (Figure 10A−C,F).

These initial results confirm the effect of the $A_{2B}AR$ antagonists optimized here at the immune system level and their potential in the context of cancer immunotherapy. Further studies are ongoing in our laboratories to elucidate and obtain a comprehensive view of the immunological signature of $A_{2B}AR$ antagonists.

CONCLUSIONS

A large collection of pyrimidine-based $A_{2B}AR$ antagonists was obtained and evaluated as part of our program aimed to unravel the therapeutic potential of blocking $A_{2B}AR$ in the context of cancer (immuno)therapy. Eight new $A_{2B}AR$ antagonists, combining notable affinity (K_i < 10 nM) and attractive subtype selectivity, were identified during the assessment of the impact of (di- and mono-)halogenation at positions 7 and 8 on the $A_{2B}AR$ affinity in a series of alkyl 7/8-halo-4-heteroaryl-1,4-dihydro-benzo[4,5]-imidazo[1,2-*a*]-pyrimidine-3-carboxylates. The study showed that introduction of two halogen atoms (at positions 7 and 8) and the halogenation at position 7 produced an important, halogen-size-dependent, decay in $A_{2B}AR$ affinity. In clear contrast, halogenation at position 8 produced potent $A_{2B}AR$ ligands irrespective of the nature of the halogen. The SAR trends observed here were substantiated by a structure-based molecular modeling study including FEP simulations. The project also provided additional evidence supporting the importance of the stereodisposition of the pentagonal ring at position 4 on the $A_{2B}AR$ affinity, with some eutomers eliciting sub-nanomolar $A_{2B}AR$ affinity and retaining the remarkable subtype selectivity. As part of this study was identified the first example of a dual $A_{2A}/A_{2B}AR$ antagonist exhibiting a stereoselective recognition at $A_{2A}AR$ and $A_{2B}AR$. The func-

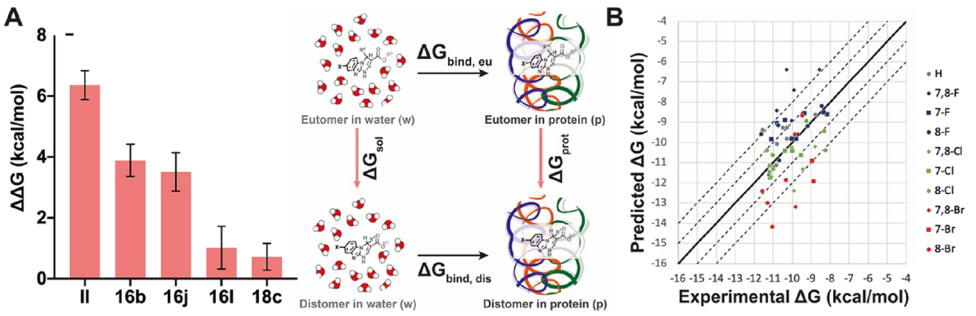

Figure 8. (A) ΔΔG data for eutomer to distomer transition (positive ΔΔG). (B) ΔG FEP correlation between all compounds showing K_i in pharmacology experimental assays, grouped by position and halogen.

https://doi.org/10.1021/acs.jmedchem.2c01768
J. Med. Chem. 2023, 66, 890−912

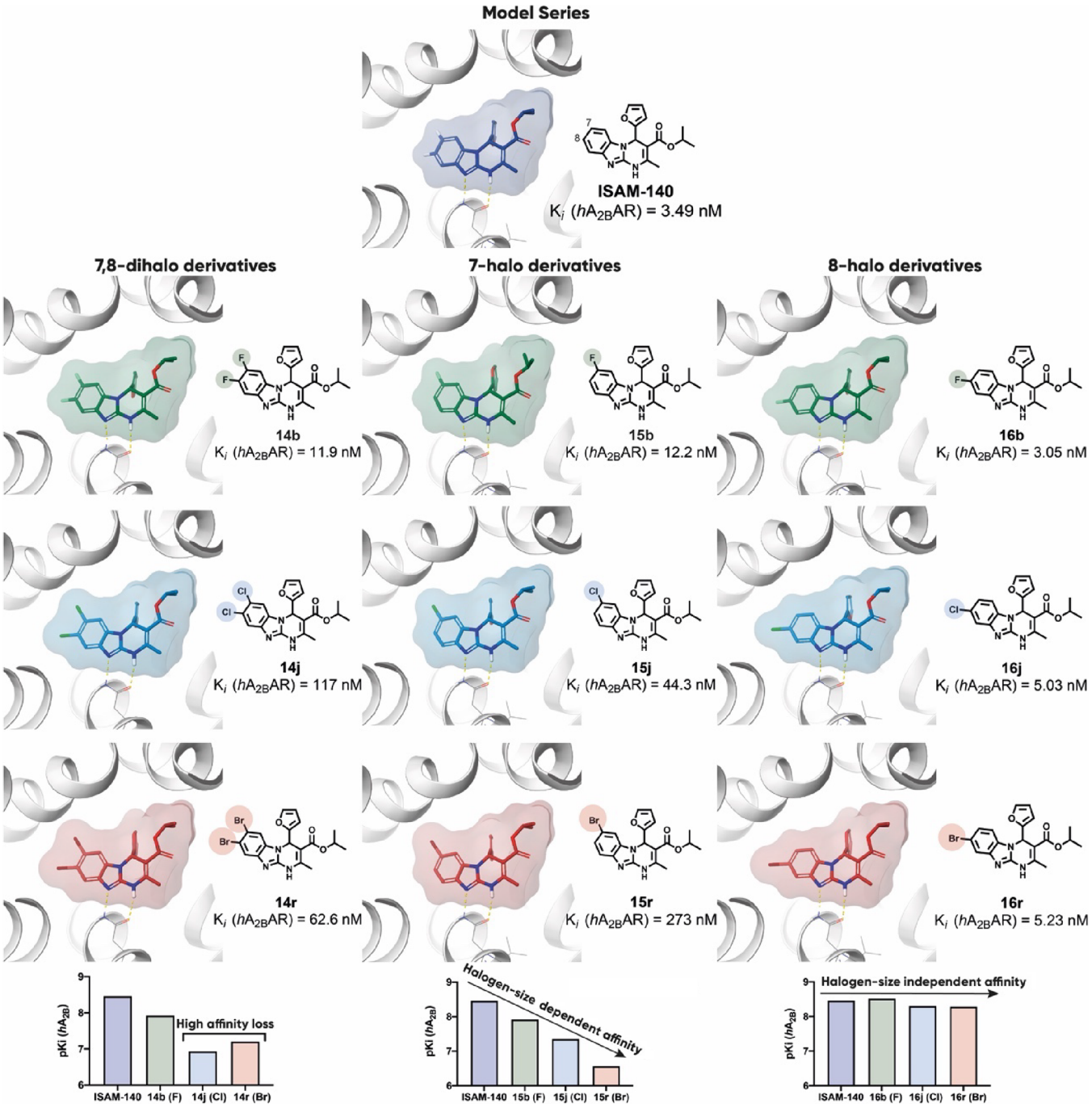

Figure 9. Docking pose for series **I** (7,8-dihalo derivatives, left), series **II** (7-halo derivatives, center), and **III** (8-halo derivatives, right), shown for the subset of derivatives with R^4 = 2-furyl and R^3 = *i*-Pr, together with their affinity profile at $A_{2B}AR$ (homology model from $A_{2A}AR$, PDB: 3EML).

tional profile of representative ligands as $A_{2B}AR$ antagonists was confirmed by cAMP-based assays. Evaluation of different ADME parameters enabled to verify the benefits of the halogenation but also to identify lead compounds combining improved affinity and selectivity and a good PK profile. Finally, two ligands optimized here unequivocally reversed the Ado-mediated antiproliferative effect on human PBMCs, thus highlighting their potential in the context of cancer immunotherapy.

EXPERIMENTAL SECTION

Chemistry. All starting materials, reagents, and solvents were purchased and used without further purification. After extraction from aqueous phases, the organic solvents were dried over anhydrous magnesium sulfate. The reactions were monitored by TLC on 2.5 mm Merck silica gel GF 254 strips, and the purified compounds each showed a single spot. Unless stated otherwise, UV light and/or iodine vapor were used to detect compounds. The Biginelli reactions were performed in coated Kimble vials on a PLS (6 × 4) Organic Synthesizer with orbital stirring or Anton Paar Microwave Synthesis Reactor. The purity and identity of all tested compounds were established by a combination of HPLC, mass spectrometry, and NMR spectroscopy as described in the Supporting Information. Purification of isolated products was carried out by column chromatography (Kieselgel 0.040−0.063 mm, E. Merck) or medium-pressure liquid chromatography (MPLC) on a Combi Flash Companion (Teledyne ISCO) with RediSep pre-packed normal-phase silica gel (35−60 μm)

https://doi.org/10.1021/acs.jmedchem.2c01768
J. Med. Chem. 2023, 66, 890−912

Table 8. Preliminary ADME and Binding Data of Novel and Previously Reported $A_{2B}AR$ Antagonists

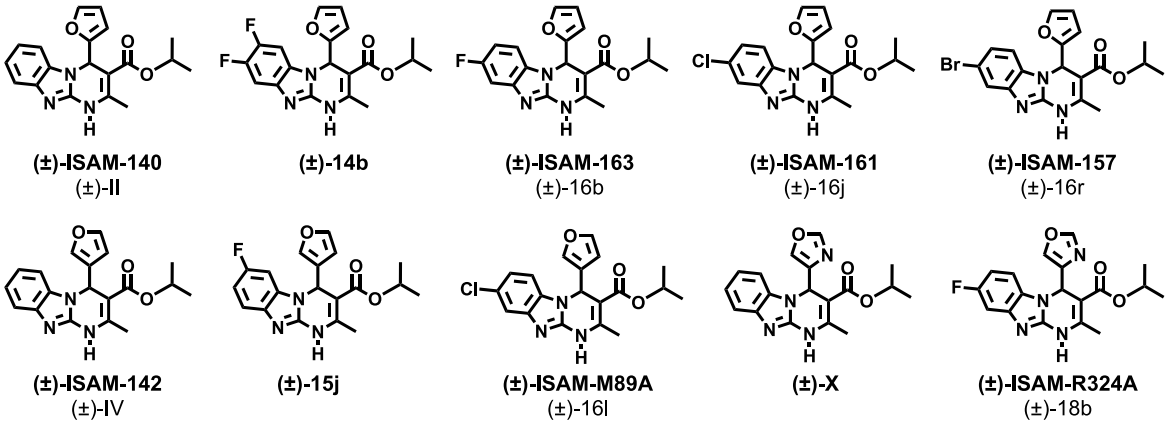

		microsomal stability			CYP3A4 IC_{50} (μM)[e] or % inh. at 10 μM[f]		
compound	solubility (μM)[a]	percent[b]	$t_{1/2}$[c]	Cl_{int}[d]	DBF	7-BFC	$hA_{2B}K_i$ (nM)
II (ISAM-140)[30]	**25.2**				**2.90 ± 0.37**		**3.49 ± 0.2**
14b	62.0	20.97	28.93	21.65	>10 (39%)	>10 (58%)	11.9 ± 1.1
16b (ISAM-163)	47.5	19.83	27.40	20.07	>10 (40%)	>10 (63%)	3.05 ± 0.7
16j (ISAM-161)	23.7	22.75	28.14	18.60	3.68 ± 0.47	>10 (54%)	5.03 ± 0.3
16r (ISAM-157)	70.7	32.13	36.79	14.23	2.26 ± 0.30	>10 (52%)	5.23 ± 0.4
IV (ISAM-142)[30]	**26.1**				**2.68 ± 0.53**		**11.4 ± 0.5**
15j	58.2	16.83	21.13	26.44	>10 (47%)	>10 (11%)	44.3 ± 1.4
16l (ISAM-M89A)	21.9	41.02	44.80	11.68	6.36 ± 1.02	>10 (44%)	6.10 ± 0.7 (A_{2B}) 176 ± 4 (A_{2A})
X[31]	**39.7**				**5.92 ± 0.68**		**43.4 ± 1.3**
18b (ISAM-R324A)	64.6	35.15	40.8	12.83	>10 (31%)	>10 (52%)	6.10 ± 0.3
PSB-603[28]	0.2						0.553
progesterone	6.7						
prazosin	31.3						
testosterone		7.11	16.13	32.44			
ketoconazole					0.008 μM	0.027 μM	

[a]Solubility in 1:99 DMSO/PSB buffer. [b]Percentage remanent (sampling time 60 min). [c]$t_{1/2}$ in min. [d]Intrinsic clearance in microliters per minute per milligram of protein. [e]IC_{50} value obtained by extrapolation with analysis software. [f]Due the low activity shown at CYP3A4, the percentage of inhibition at 10 μM is reported.

columns followed by recrystallization. Melting points were determined on a Stuart Scientific melting point apparatus and are uncorrected. The NMR spectra were recorded on Bruker AM300 and XM500 spectrometers. Chemical shifts are given as δ values against tetramethylsilane as internal standard, and J values are given in Hertz. Mass spectra were obtained on a Varian MAT 711 instrument. For regioisomer differentiation experiments, ^{1}H NMR, 2D-ROESY, and 2D-NOESY were recorded on an AV NEO 750 MHz instrument. High-resolution mass spectra were obtained on an AutoSpec Micromass spectrometer. Analytical HPLC was performed on a Water Breeze 2 system (binary pump 1525, detector UV/Visible 2489, 7725i Manual Injector Kit 1500 Series) using a Luna 5 μm Silica (2) 100 Å, LC Column 150 × 4.6 mm column with gradient elution using the mobile phases dichloromethane, isopropanol, and a flow rate of 1 mL/min. The purity of all tested compounds was determined to be >95%.

The chiral resolution was performed using a Water Breeze 2 (binary pump 1525, detector UV/Visible 2489, 7725i Manual Injector Kit 1500 Series). Compound **16b** enantiomers were separated using a 250 mm × 10 mm Lux 5 μm Amylose-2 (Phenomenex) while **ISAM-140**, **16j**, **16l**, **16r**, **16s**, and **18c** enantiomers were separated using a 250 mm × 20 mm CHIRALPAK 5 μm IE-3 (DAICEL). A detailed description of the experimental protocols and relevant parameters (retention times, stereochemical purities) is provided in the Supporting Information. All single stereoisomers were isolated and their stereochemical purity analyzed by chiral HPLC (>97% for each stereoisomer) and then characterized by NMR in $CDCl_3$. CD spectra were recorded on a Jasco-815 system equipped with a Peltier-type thermostatic accessory (CDF-426S, Jasco). Measurements were carried out at 20 °C using a 1 mm quartz cell in a volume of 300−350 mL. Compounds (0.1 mg) were dissolved in MeOH (1.0 mL). The instrument settings were bandwidth, 1.0 nm; data pitch, 1.0 nm; speed, 500 nm/min; accumulation, 10; and wavelengths, 400−190 nm. A detailed description of the synthesis and structural and spectroscopic data obtained for all compounds described is provided in the Supporting Information.

*General Procedure for the Synthesis of Alkyl 7,8-dihalobenzo-[4,5]imidazo[1,2-a]pyrimidine-3-carboxylates **14a−x**.* (Method A): A mixture of the corresponding 5,6-dihalo-2-aminobenzimidazole **11a−c** (1.5 equiv), aldehyde **12a−d** (1 equiv), β-ketoester **13a,b** (1 equiv), and $ZnCl_2$ (0.1 equiv) in THF (2.5 mL) was stirred with orbital stirring at 90 °C for 12 h. After completion of the reaction, as indicated by TLC, the solvent was removed in vacuum and the obtained oily residue was purified by column chromatography on silica gel, obtaining the corresponding alkyl 7,8-dihalobenzo[4,5]-imidazo[1,2-*a*]pyrimidine-3-carboxylates (**14a−x**).

*General Procedure for the Synthesis of Alkyl 7-halobenzo[4,5]-imidazo[1,2-a]pyrimidine-3-carboxylates **15a−x** and 8-Halobenzo[4,5]imidazo[1,2-a]pyrimidine-3-carboxylates **16a−x**.* (Method A): A mixture of 2-amino-5-halobenzimidazole **11d−f** (1.5 equiv), aldehyde **12a−d** (1 equiv), β-ketoester **13a,b** (1 equiv), and $ZnCl_2$ (0.1 equiv) in THF (2.5 mL) was stirred with orbital stirring at 90 °C for 12 h. After completion of the reaction, as indicated by TLC, the solvent was removed in vacuum and the obtained oily residue was purified by column chromatography on

https://doi.org/10.1021/acs.jmedchem.2c01768
J. Med. Chem. 2023, 66, 890−912

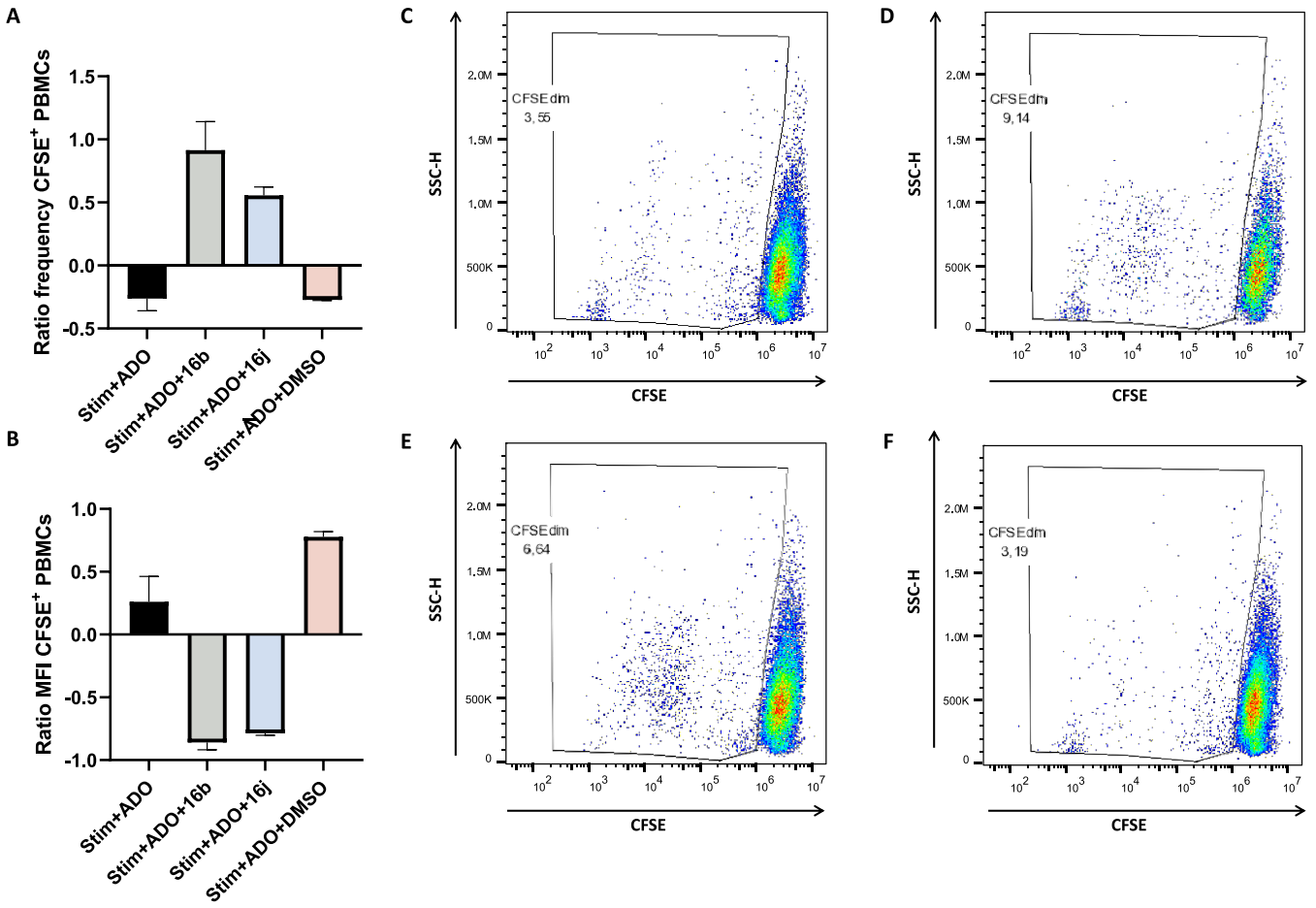

Figure 10. Effect of compounds **16b** and **16j** on the proliferation of PBMCs stimulated with antiCD3/CD28 + IL-2 in the presence of adenosine (ADO). PBMCs were CFSE-labeled, stimulated with anti-CD3/CD28 antibodies and IL-2, and cultured with the compounds of interest in the presence of adenosine for 3 days. The frequency of proliferating cells ($CFSE^{dim}$) as well as their median fluorescence intensities were quantified and ratios calculated against the values of stimulated PBMCs with no further treatment. (A) Frequency of proliferating cells. (B) MFI of proliferating cells. (C–F) Representative dots plots of the proliferation of CFSE-stained PBMCs treated with anti-CD3/CD28 + IL-2 + ADO (C), anti-CD3/CD28 + IL-2 + ADO +16b (D), anti-CD3/CD28 + IL-2 + ADO +16j (E), and anti-CD3/CD28 + IL-2 + ADO + DMSO (F).

silica gel, obtaining the corresponding alkyl 7- and 8-halobenzo[4,5]-imidazo[1,2-*a*]pyrimidine-3-carboxylates.

*General Procedure for the Synthesis of Alkyl 7-Halo-4-(oxazol-4-yl)-benzo[4,5]imidazo[1,2-a]pyrimidine-3-carboxylates **17a–d** and 8-Halo-4-(oxazol-4-yl)-benzo[4,5]imidazo[1,2-a]pyrimidine-3-carboxylates **18a–d**.* (Method B): A mixture of 2-amino-5-halobenzimidazole **11d,e** (1.5 equiv), oxazole-4-carbaldehyde **12e** (1 equiv), *β*-ketoester **13a,b** (1 equiv), and AcOH (three drops) in THF (2 mL) and DMF (1 mL) was stirred under microwave irradiation at 80 °C for 90 min. After completion of the reaction, as indicated by TLC, the solvent was removed in vacuum and the obtained oily residue was purified by column chromatography on silica gel, obtaining the corresponding alkyl 7- and 8-halo-4-(oxazol-4-yl)-benzo[4,5]imidazo-[1,2-*a*]pyrimidine-3-carboxylates (**17a–d** and **18a–d**).

Pharmacology Binding Assays. Radioligand binding competition assays were performed in vitro using human ARs expressed in transfected HeLa [$h$$A_{2A}$AR (9 pmol/mg protein) and $h$$A_3$AR (3 pmol/mg protein)], HEK-293 [$h$$A_{2B}$AR (1.5 pmol/mg protein)], and CHO [$h$$A_1$AR (1.5 pmol/mg protein)] cells as described previously.[25,31,33] A brief description is given below. A_1AR competition binding experiments were carried out in membranes from CHO-A_1 cells labeled with 1 nM [^{3}H]DPCPX (K_D = 0.7 nM). Non-specific binding was determined in the presence of 10 μM R-PIA. The reaction mixture was incubated at 25 °C for 60 min. A_{2A}AR competition binding experiments were carried out in membranes from HeLa-A_{2A} cells labeled with 3 nM [^{3}H]ZM241385 (K_D = 2 nM). Non-specific binding was determined in the presence of 50 μM NECA. The reaction mixture was incubated at 25 °C for 30 min. A_{2B}AR competition binding experiments were carried out in membranes from HEK-293-A_{2B} cells (Euroscreen, Gosselies, Belgium) labeled with 25 nM [^{3}H]DPCPX (K_D = 21 nM). Non-specific binding was determined in the presence of 400 μM NECA. The reaction mixture was incubated at 25 °C for 30 min. A_3AR competition binding experiments were carried out in membranes from HeLa-A_3 cells labeled with 10 nM [^{3}H]NECA (K_D = 8.7 nM). Non-specific binding was determined in the presence of 100 μM R-PIA. The reaction mixture was incubated at 25 °C for 180 min. After the incubation time, membranes were washed and filtered and radioactivity was detected in a MicroBeta TriLux reader (PerkinElmer).

Pharmacology Functional Experiments. *Reagents.* The following reagents were used: adenosine deaminase (ADA, Roche Diagnostics, Mannheim, Germany), 5′-*N*-ethylcarboxamidoadenosine (NECA, Tocris, Bristol, UK), zardaverine (Calbiochem, San Diego, California, USA), SNAP-Surface Alexa Fluor 488 (New England BioLabs, Ipswich, Massachusetts, USA).

Cloning. The cDNA encoding the human A_{2B}AR was amplified by polymerase chain reaction using the primers FA2BREcoRV (5′-tcgag**GATATC**CTGCTGGAGACACAGGACGC-3′) and RA2BR-HindIII (5′-cgag**AAGCTT**TCATAGGCCCACACCGAGAGC-3′) and subcloned into the *Eco*RV/*Hind*III restriction sites of the pRK5-A_1R^{SNAP} vector (kindly provided by Dr. J. P. Pin, Université de Montpellier and Institut de Génomique Fonctionnelle, Montpellier, France) by replacing the Ado A_1 receptor. The resulting construct encoded the human A_{2B}AR tagged with SNAP, a 20 kDa

https://doi.org/10.1021/acs.jmedchem.2c01768
J. Med. Chem. 2023, 66, 890–912

mutant of the DNA repair protein O^6-alkylguanine-DNA alkyltransferase (AGT), at its N-terminus (pRK5-$A_{2B}AR^{SNAP}$).

Cell Culture and Stable Transfection. Human embryonic kidney (HEK)-293 T cells were grown in Dulbecco's modified Eagle's medium (DMEM) (Sigma-Aldrich, St. Louis, Missouri, USA) supplemented with 1 mM sodium pyruvate (Biowest, Nuaillé, France), 2 mM L-glutamine (Biowest), 100 U/mL streptomycin (Biowest), 100 mg/mL penicillin (Biowest), and 5% (v/v) fetal bovine serum (Invitrogen, Carlsbad, California, USA) at 37 °C and in an atmosphere of 5% CO_2. HEK-293 cells growing in 60 cm^2 plates were transfected with pRK5-$A_{2B}AR^{SNAP}$ using the polyethylenimine (PEI) method.[53] After 48 h of transfection, cells were stained using SNAP-Surface Alexa Fluor 488.[38] Fluorescent cells were selected every 2 weeks for 2 months using a Cell sorter (MoFlo Astrios, Beckman Coulter) to enrich the percentage of cells that express the receptor, thus ensuring its permanent expression.[54]

cAMP Accumulation Assay. cAMP accumulation was measured using the LANCE Ultra cAMP kit (PerkinElmer, Waltham, Massachusetts, USA) as previously described.[55] In brief, HEK-293 T cells permanently expressing the $A_{2B}AR^{SNAP}$ construct ($A_{2B}AR^{SNAP}$ cells) were detached with Accutase (Sigma-Aldrich) and incubated for 1 h at 22 °C in Dulbecco's modified Eagle's medium (DMEM) (Sigma-Aldrich) supplemented with 0.1% BSA, ADA (0.5 U/mL), and zardaverine (100 μM). $A_{2B}AR^{SNAP}$ cells (1×10^4 cells/200 μL) were incubated with NECA in the presence/absence of increasing concentrations of **16b**, **16j**, **16r**, and **16s**, during 30 min at 22 °C. Eu-cAMP tracer and ULight-anti-cAMP reagents were prepared and added to the sample following the manufacturer's instructions. The 384-well plate was incubated 1 h at 22 °C in the dark and was then read on a CLARIOstar Microplate Reader (BMG Labtech, Durham, North Carolina, USA). Measurements at 620 and 665 nm were used to detect the TR-FRET signal, and the concomitant cAMP levels were calculated following the manufacturer's instructions. Data were fitted by non-linear regression using GraphPad Prism 9 (San Diego, California, USA).

Concentration−response curves were carried out by assaying different **16b**, **16j**, **16r**, and **16s** concentrations ranging between 10 nM and 30 μM. Data was expressed as K_B by following the formula reported by Leff and Dougall (eq 1):[56]

$$K_B = \frac{IC_{50}}{\left(2 + \left(\frac{[A]}{[A_{50}]}\right)^n\right)^{1/n}} \quad (1)$$

Correction offset value for all the ABFE estimates.[56]

where IC_{50} is the concentration of compound that inhibits NECA effect by 50%, $[A]$ is the concentration of NECA employed in the assay, $[A_{50}]$ is the NECA EC_{50} value, and n is the Hill slope of the curve.

Cellular Impedance Label-Free Assay. The xCELLigence RTCA system (Roche) was employed to assess the impact of blocking $A_{2B}AR$-mediated effects in cellular impedance upon receptor activation, as previously described.[57−60] To this end, $A_{2B}AR^{SNAP}$ cells were growth in 16-well E-plates (Roche), using DMEM supplemented with 1 mM sodium pyruvate, 2 mM L-glutamine, 100 U/mL streptomycin, 100 mg/mL penicillin, and 1.5% (v/v) fetal bovine serum in the presence of 0.5 U/mL of ADA. Of note, wells were previously coated with 50 μL fibronectin (10 μg/mL; Sigma-Aldrich) and the background index for each well was determined with supplemented DMEM (90 μL) in the absence of cells. Subsequently, $A_{2B}AR^{SNAP}$ cells (90 μL) were plated at a cell density of 10,000 cells/well and grown for 18 h in the RTCA SP device station (Roche) at 37 °C in an atmosphere of 5% CO_2. Then, before ligand addition, cell index values were normalized to the same time point using the RTCA software, providing the normalized cell index (NCI). After ligand stimulation, NCI was recorded every 15 s for a total time of at least 45 min. The area under the curve (AUC) for every condition was calculated using GraphPad Prism 9.

Data and Statistical Analysis. Data are represented as mean ± standard error of mean (SEM) with statistical significance set at $P < 0.05$. The number of samples (n) in each experimental condition is indicated in the corresponding figure legend. Outliers were assessed by the ROUT method;[61] thus, any sample was excluded assuming a Q value of 1% in GraphPad Prism 9 (San Diego, California, USA). Comparisons among experimental groups were performed by the Student t test or one-way analysis of variance (ANOVA) followed by Tukey's multiple-comparison post hoc test using GraphPad Prism 9, as indicated.

CYP3A4 Inhibition. The inhibitory activity of selected compounds was evaluated by following a previously described method.[31] Incubations were conducted in a 200 μL volume in 96-well microtiter plates (Costar 3915). Addition of a cofactor−buffer mixture (KH_2PO_4 buffer, 1.3 mM NADP, 3.3 mM $MgCl_2$, 3.3 mM glucose-6-phosphate, and 0.4 U/mL glucose-6-phosphate dehydrogenase), supersome control, standard inhibitor (ketoconazole from Sigma-Aldrich) previously diluted, and compounds to plates were carried out by a liquid handling station (Zephyr Caliper). The plate was then pre-incubated at 37 °C for 5 min and the reaction initiated by the addition of a pre-warmed enzyme/substrate (E/S) mix. The E/S mix contained buffer (KH_2PO_4), c-DNA-expressed P450 in insect cell microsomes, substrate (DBF: dibenzylfluorescein or 7-BFC: 7-benzyloxy-4-trifluoromethyl-coumarin) and other components to give the final assay concentrations in a reaction volume of 200 μL. Reactions were terminated after various times (a specific time for each cytochrome) by addition of STOP solution (ACN/Tris−HCl 0.5 M 80:20, and NaOH 2 N for CYP3A4). Fluorescence per well was measured using a fluorescence plate reader (Tecan Infinite M1000 PRO), and percentage of inhibition was calculated. In silico predictions were performed using free web-based models (FAME 3, SmartCYP, and Xenosite).[62−64]

Human Microsomal Stability. The human microsomal stability of selected compounds was evaluated by following a previously described method.[31] The human microsomes employed were purchased from Tebu-Xenotech. The compound was incubated with the microsomes at 37 °C in a 50 mM phosphate buffer (pH = 7.4) containing 3 mM $MgCl_2$, 1 mM NADP, 10 mM glucose-6-phosphate, and 1 U/mL glucose-6-phosphate-dehydrogenase. Samples (75 μL) were taken from each well at 0, 10, 20, 40, and 60 min and transferred to a plate containing 4 °C 75 μL acetonitrile and 30 μL of 0.5% formic acid in water was added for improving the chromatographic conditions. The plate was centrifuged (46,000 g, 30 min), and supernatants were taken and analyzed in a UPLC-MS/MS (Xevo TQD, Waters) by employing a BEH C18 column and an isocratic gradient of 0.1% formic acid in water:0.1% formic acid acetonitrile (60:40). The metabolic stability of the compounds was calculated from the logarithm of the remaining compounds at each of the time point studied.

Solubility Determinations. The solubility of selected compounds was evaluated by following a previously described method.[31] A 10 mM stock solution of the compound was serially diluted in 100% DMSO, and 2.5 μL of this solution was added to a 384-well UV-transparent plate (Greiner) containing 47.5 μL of PBS (pH = 7). The plate was incubated at 37 °C for 4 h, and the light scattering was measured in a NEPHELOstar Plus reader (BMG LABTECH). The data was fitted to a segmented linear regression for measuring the compound solubility.

System Preparation and MD/FEP Simulations. The structural model for the $A_{2B}AR$ receptor derives from a homology model previously reported[31,33] and here processed using the Protein Preparation Wizard pipeline in Maestro (Schrodinger ver. 2021-3). Subsequently, possible 3D tautomers and protomers at pH 7 ± 2 were generated for each compound using the OPLS4 force field[65] and Epik, the lowest energy conformer was chosen for molecular docking. A receptor grid was generated with the default Van der Waals radius scaling settings, and it was positioned in the center of geometry of the binding site. Thereafter, Glide SP docking was performed leading to the protein−ligand complexes, which were used as the starting point for the MD/FEP simulations carried out with the software package Q.[66] An FEP network was generated for each of chemical series using ECFP4 as a measure of the chemical similarity between ligand pairs,

https://doi.org/10.1021/acs.jmedchem.2c01768
J. Med. Chem. 2023, 66, 890−912

ensuring smooth alchemical transformations while covering the entire dataset. For each vertex comparing a pair of compounds part of the FEP network, the QligFEP[67] pipeline was used for generating the MD/FEP input files and its posterior analysis. The MD simulations were carried out under spherical boundary conditions (SBC) with a sphere size of 25 Å, with solvent atoms lying in the outer shell of the sphere (22−25 Å) subject to radial and polarization restrains using the surface-constrained all-atom solvent (SCAAS).[68,69] All titratable residues outside the sphere were neutralized, and histidine protonation states were set by the Protein Preparation Wizard. Atoms outside the simulation sphere were excluded from the calculation of the nonbonded interactions and tightly constrained (200 kcal/mol·Å^2) to its position. Long-range electrostatic interactions beyond a 10 Å threshold were evaluated using the local reaction field method,[68] excluding the atoms undergoing the FEP transformation where no cut-off is applied. The OPLS-AA/M force field[70] was used for the protein and solvent (TIP3P) parameters, while OPLS2005 ligand parameters were generated using the ffld_server;[71] solvent bonds and angles were constrained using the SHAKE algorithm.[72] The MD/FEP simulations are preceded by a heating phase of the sphere from 0.1 to 298 K during a short 31 ps stage where a positional restraint of 10 kcal/mol·Å^2 is progressively released. This is followed by a 100 ps unbiased and unrestrained equilibration, and subsequently, MD sampling is performed across a predefined sigmoidal λ schedule, consisting of 101 λ windows, each consisting of 10 ps sampling using a 2 fs timestep. To get initial relative binding free energy estimates (RBFE), the thermodynamic cycles are closed for each ligand pair defined in the FEP network by performing the corresponding MD/FEP simulation in a water sphere, and the free energies are calculated with the Bennet acceptance ratio (BAR) method.[66] The cycle closure correction framework[73] was utilized for assessing the convergence of the initial RBFE estimates, and additionally, it yielded corrected RBFE values, which eliminate the hysteresis along all the thermodynamic cycles encompassed by the FEP network. To get the ABFE for all the compounds of interest, the corrected RBFE values together with the FEP networks and the experimental binding free energy for a reference compound per network are used. The Bellman−Ford implementation from NetworkX[74] was used for finding the shortest path connecting a reference with the remaining target compounds, and, for each target compound, eq 1 was used to get the ABFE estimates. Finally, a correction offset value for all the ABFE estimates was calculated as described by Wang et al.[75] in order to minimize the experimental error introduced to the final estimates (eq 2).

$$\Delta G_{\text{pred}}^{\text{Targ.comp.}} = \Delta G_{\text{exp}}^{\text{Ref.comp.}} + \sum_{i=1}^{N} \Delta\Delta G_{\text{pred}}^{\text{FEP},i} \quad (2)$$

Correction offset value for all the ABFE estimates.[75]

In Vitro Evaluation of the Immunostimulatory Effect. PBMCs were isolated from a healthy donor, stained with CFSE (Abcam) following the manufacturer's protocol, and cultured in duplicates in U-bottom 96-well plates at a density of 1.5 × 10^5 cells/well in RPMI 1640 medium (Gibco) supplemented with 10% AB Human Serum (Sigma-Aldrich) and 1% penicillin−streptomycin (Gibco). PBMCs were stimulated with ImmunoCult Human CD3/CD28 T Cell Activator (STEMCELL Technologies) and 50 U/mL Interleukin 2 (Gibco). Ado was then added at a final concentration of 0.1 mM and compounds **16b** and **16j** at 15 μM. DMSO was used as vehicle control. PBMCs were kept in culture with the different treatments for 3 days in an incubator at 37 °C and 5% CO_2. After the culture period, cells were washed twice with DPBS (Gibco) and CFSE fluorescence measured in a BD Accuri flow cytometer. The data was analyzed using FlowJo software (BD): the percentage of CFSE$^+$ cells, and their median fluorescence intensity (MFI) was quantified for each treatment condition, and a ratio against the stimulated condition without Ado was calculated for each treatment. Positive values indicate increases in the variable compared to the stimulated control, while negative values indicate decreases in the measured variable.

■ ASSOCIATED CONTENT

Supporting Information

The Supporting Information is available free of charge at https://pubs.acs.org/doi/10.1021/acs.jmedchem.2c01768.

Molecular formula strings (CSV)

Atomic coordinates and experimental data upon article publication (ZIP)

Spectroscopic and analytical data for all compounds described, HPLC enantiomeric separations, X-ray crystallography assays, supplementary figures, supplementary tables, and HPLC traces for lead compounds (PDF)

■ AUTHOR INFORMATION

Corresponding Authors

José Brea − *Center for Research in Molecular Medicine and Chronic Diseases (CiMUS) and Department of Pharmacology, Pharmacy and Pharmaceutical Technology, Faculty of Pharmacy, University of Santiago de Compostela, 15782 Santiago de Compostela, Spain;* orcid.org/0000-0002-5523-1979; Phone: +34 881815459; Email: pepo.brea@usc.es; Fax: +34-8818115474

Hugo Gutiérrez-de-Terán − *Department of Cell and Molecular Biology, Uppsala University, 75124 Uppsala, Sweden;* orcid.org/0000-0003-0459-3491; Phone: +46 18 471 5056; Email: hugo.gutierrez@icm.uu.se; Fax: +46 18 536971

Eddy Sotelo − *Center for Research in Biological Chemistry and Molecular Materials (CIQUS) and Department of Organic Chemistry, Faculty of Pharmacy, University of Santiago de Compostela, 15782 Santiago de Compostela, Spain;* orcid.org/0000-0001-5571-2812; Phone: +34 881815732; Email: e.sotelo@usc.es; Fax: +34-881815704

Authors

Rubén Prieto-Díaz − *Center for Research in Biological Chemistry and Molecular Materials (CIQUS) and Department of Organic Chemistry, Faculty of Pharmacy, University of Santiago de Compostela, 15782 Santiago de Compostela, Spain; Department of Cell and Molecular Biology, Uppsala University, 75124 Uppsala, Sweden;* orcid.org/0000-0003-2539-3106

Manuel González-Gómez − *Center for Research in Biological Chemistry and Molecular Materials (CIQUS) and Department of Organic Chemistry, Faculty of Pharmacy, University of Santiago de Compostela, 15782 Santiago de Compostela, Spain*

Hugo Fojo-Carballo − *Center for Research in Biological Chemistry and Molecular Materials (CIQUS) and Department of Organic Chemistry, Faculty of Pharmacy, University of Santiago de Compostela, 15782 Santiago de Compostela, Spain*

Jhonny Azuaje − *Center for Research in Biological Chemistry and Molecular Materials (CIQUS) and Department of Organic Chemistry, Faculty of Pharmacy, University of Santiago de Compostela, 15782 Santiago de Compostela, Spain*

Abdelaziz El Maatougui − *Center for Research in Biological Chemistry and Molecular Materials (CIQUS) and Department of Organic Chemistry, Faculty of Pharmacy, University of Santiago de Compostela, 15782 Santiago de Compostela, Spain*

Maria Majellaro − *Center for Research in Biological Chemistry and Molecular Materials (CIQUS) and Department of Organic Chemistry, Faculty of Pharmacy, University of Santiago de Compostela, 15782 Santiago de Compostela, Spain*

María I. Loza − *Center for Research in Molecular Medicine and Chronic Diseases (CiMUS) and Department of Pharmacology, Pharmacy and Pharmaceutical Technology, Faculty of Pharmacy, University of Santiago de Compostela, 15782 Santiago de Compostela, Spain;* orcid.org/0000-0003-4730-0863

Víctor Fernández-Dueñas − *Pharmacology Unit, Department of Pathology and Experimental Therapeutics, Faculty of Medicine and Health Sciences, Institute of Neuroscience, University of Barcelona, 08907 L'Hospitalet de Llobregat, Spain; Neuropharmacology and Pain Group, Neuroscience Program, Institut d'Investigació Biomèdica de Bellvitge, IDIBELL, 08907 L'Hospitalet de Llobregat, Spain*

M. Rita Paleo − *Center for Research in Biological Chemistry and Molecular Materials (CIQUS) and Department of Organic Chemistry, Faculty of Pharmacy, University of Santiago de Compostela, 15782 Santiago de Compostela, Spain;* orcid.org/0000-0002-0095-3931

Alejandro Díaz-Holguín − *Department of Cell and Molecular Biology, Uppsala University, 75124 Uppsala, Sweden*

Beatriz Garcia-Pinel − *Center for Research in Molecular Medicine and Chronic Diseases (CiMUS) and Department of Biochemistry and Molecular Biology, Faculty of Pharmacy, University of Santiago de Compostela, 15782 Santiago de Compostela, Spain;* orcid.org/0000-0002-4473-7659

Ana Mallo-Abreu − *Center for Research in Biological Chemistry and Molecular Materials (CIQUS) and Department of Organic Chemistry, Faculty of Pharmacy, University of Santiago de Compostela, 15782 Santiago de Compostela, Spain;* orcid.org/0000-0002-5092-3538

Juan C. Estévez − *Center for Research in Biological Chemistry and Molecular Materials (CIQUS) and Department of Organic Chemistry, Faculty of Pharmacy, University of Santiago de Compostela, 15782 Santiago de Compostela, Spain;* orcid.org/0000-0001-9468-9045

Antonio Andújar-Arias − *Center for Research in Biological Chemistry and Molecular Materials (CIQUS) and Department of Organic Chemistry, Faculty of Pharmacy, University of Santiago de Compostela, 15782 Santiago de Compostela, Spain;* orcid.org/0000-0001-9922-3543

Xerardo García-Mera − *Department of Organic Chemistry, Faculty of Pharmacy, University of Santiago de Compostela, 15782 Santiago de Compostela, Spain*

Iria Gomez-Tourino − *Center for Research in Molecular Medicine and Chronic Diseases (CiMUS), University of Santiago de Compostela, 15782 Santiago de Compostela, Spain*

Francisco Ciruela − *Pharmacology Unit, Department of Pathology and Experimental Therapeutics, Faculty of Medicine and Health Sciences, Institute of Neuroscience, University of Barcelona, 08907 L'Hospitalet de Llobregat, Spain; Neuropharmacology and Pain Group, Neuroscience Program, Institut d'Investigació Biomèdica de Bellvitge, IDIBELL, 08907 L'Hospitalet de Llobregat, Spain;* orcid.org/0000-0003-0832-3739

Cristian O. Salas − *Department of Organic Chemistry, Faculty of Chemistry and Pharmacy, Pontificia Universidad Católica de Chile, Santiago 7820436, Chile*

Complete contact information is available at: https://pubs.acs.org/10.1021/acs.jmedchem.2c01768

Notes

The authors declare no competing financial interest.

■ ACKNOWLEDGMENTS

This work was financially supported by the Consellería de Cultura, Educación e Ordenación Universitaria of the Galician Government (grant: ED431B 2020/43), Centro Singular de Investigación de Galicia accreditation 2019-2022 (ED431G 2019/03), the European Regional Development Fund (ERDF), Ministerio de Ciencia e Innovación − Agencia Estatal de Investigación-FEDER-UE (PID2020-118511RB-I00 and PID2021-124010OB-100). Additional support from the Swedish strategic research program eSSENCE, the Swedish Cancer Society (#CAN 2018/451), and The Cancer Research Fundations of Radiumhemmet (#181183) is acknowledged. The computations were performed on resources provided by the Swedish National Infrastructure for Computing (SNIC). We thank Centres de Recerca de Catalunya (CERCA) Programme/Generalitat de Catalunya for IDIBELL institutional support, Xunta de Galicia (ED431C 2018/21 and ED431G 2019/02), and European Regional Development Fund (ERDF) in the frame of the Recovery Assistance for Cohesion and the Territories of Europe (REACT-EU) funds. This research program has been developed in the frame of the European COST action ERNEST (CA 18133).

■ ABBREVIATIONS

ABFE, absolute binding free energies; ADMET, absorption, distribution, metabolism, excretion, and toxicity; Ado, adenosine; AGT, O^6-alkylguanine-DNA alkyltransferase; AR, adenosine receptor; AUC, area under curve; cAMP, cyclic adenosine monophosphate; CD, circular dichroism; CFSE, carboxyfluorescein succinimidyl ester; CHO, Chinese hamster ovary; Cmpd, compound; Cmpds, compounds; DMEM, Dulbecco's modified Eagle's medium; DMF, dimethylformamide; DPCPX, dipropylcyclopentyl-xanthine; FEP, free energy perturbation; GPCRs, G protein-coupled receptors; MD, molecular dynamics; MFI, median fluorescence intensities; MPLC, medium pressure liquid chromatography; NECA, *N*-ethoxycarbonyl adenosine; NMR, nuclear magnetic resonance; P_1, class 1 purinergic receptors; PAINS, pan-assay interference compounds; PBMCs, peripheral blood mononuclear cells; R-PIA, *R*-phenylisopropyl-adenosine; RBFE, relative binding free energies; ROESY, rotating frame Overhauser effect spectroscopy; SAR, structure−activity relationships; SBC, spherical boundary conditions; SCAAS, surface-constrained all-atom solvent; SSR, structure−selectivity relationships; THF, tetrahydrofuran; Veh, vehicle.

■ REFERENCES

(1) Borea, P. A.; Gessi, S.; Merighi, S.; Vincenzi, F.; Varani, K. Pharmacology of Adenosine Receptors: The State of the Art. *Physiol. Rev.* **2018**, *98*, 1591−1625.

(2) Fredholm, B. B. Adenosine - A Physiological or Pathophysiological Agent? *J. Mol. Med.* **2014**, *92*, 201−206.

(3) Fredholm, B. B. Adenosine, an Endogenous Distress Signal, Modulates Tissue Damage and Repair. *Cell Death Differ.* **2007**, *14*, 1315−1323.

(4) Huang, Z. L.; Zhang, Z.; Qu, W. M.*Roles of Adenosine and Its Receptors in Sleep-Wake Regulation*; 1st ed.; International Review of Neurobiology; Elsevier Inc.: 2014; Vol. *119*, p 371.
(5) Pasquini, S.; Contri, C.; Borea, P. A.; Vincenzi, F.; Varani, K. Adenosine and Inflammation: Here, There and Everywhere. *Int. J. Mol. Sci.* **2021**, *22*, 1−24.
(6) Antonioli, L.; Blandizzi, C.; Pacher, P.; Haskó, G. Immunity, Inflammation and Cancer: A Leading Role for Adenosine. *Nat. Rev. Cancer* **2013**, *13*, 842−857.
(7) Allard, B.; Allard, D.; Buisseret, L.; Stagg, J. The Adenosine Pathway in Immuno-Oncology. *Nat. Rev. Clin. Oncol.* **2020**, *17*, 611−629.
(8) Fredholm, B. B.; IJzerman, A. P.; Jacobson, K. A.; Linden, J.; Müller, C. E. International Union of Basic and Clinical Pharmacology. LXXXI. Nomenclature and Classification of Adenosine Receptors - An Update. *Pharmacol. Rev.* **2011**, *63*, 1−34.
(9) Wilson, C. N.; Jamal, S. M.Adenosine Receptors in Health and Disease. In *Handbook of Experimental Pharmacology*; Springer: Berlin, 2009; Vol. *193*, pp. 41−75.
(10) Aherne, C. M.; Kewley, E. M.; Eltzschig, H. K. The Resurgence of A2B Adenosine Receptor Signaling. *Biochim. Biophys. Acta, Biomembr.* **2011**, *1808*, 1329−1339.
(11) Vecchio, E. A.; White, P. J.; May, L. T. The Adenosine A2B G Protein-Coupled Receptor: Recent Advances and Therapeutic Implications. *Pharmacol. Ther.* **2019**, *198*, 20−33.
(12) Haskó, G.; Csóka, B.; Németh, Z. H.; Vizi, E. S.; Pacher, P. A2B Adenosine Receptors in Immunity and Inflammation. *Trends Immunol.* **2009**, *30*, 263−270.
(13) Jain, S.; Jacobson, K. A. Purinergic Signaling in Diabetes and Metabolism. *Biochem. Pharmacol.* **2021**, *187*, 114393−114404.
(14) Abo-Salem, O. M.; Hayallah, A. M.; Bilkei-Gorzo, A.; Filipek, B.; Zimmer, A.; Müller, C. E. Antinociceptive Effects of Novel A2B Adenosine Receptor Antagonists. *J. Pharmacol. Exp. Ther.* **2004**, *308*, 358−366.
(15) Popoli, P.; Pepponi, R. Potential Therapeutic Relevance of Adenosine A2B and A2A Receptors in the Central Nervous System. *CNS Neurol. Disord.-Drug Targets* **2012**, *11*, 664−674.
(16) Gao, Z.-G.; Jacobson, K. A. A2B Adenosine Receptor and Cancer. *Int. J. Mol. Sci.* **2019**, *20*, 1−18.
(17) Corona, S. P.; Sobhani, N.; Generali, D. Adenosine A2B Receptor: Novel Anti-Cancer Therapeutic Implications. *J. Cancer Metastasis Treat.* **2017**, *3*, 206−206.
(18) Antonioli, L.; Fornai, M.; Blandizzi, C.; Pacher, P.; Haskó, G. Adenosine Signaling and the Immune System: When a Lot Could Be Too Much. *Immunol. Lett.* **2019**, *205*, 9−15.
(19) Allard, B.; Beavis, P. A.; Darcy, P. K.; Stagg, J. Immunosuppressive Activities of Adenosine in Cancer. *Curr. Opin. Pharmacol.* **2016**, *29*, 7−16.
(20) Allard, D.; Turcotte, M.; Stagg, J. Targeting A2 Adenosine Receptors in Cancer. *Immunol. Cell Biol.* **2017**, *95*, 333−339.
(21) Sepúlveda, C.; Palomo, I.; Fuentes, E. Role of Adenosine A2b Receptor Overexpression in Tumor Progression. *Life Sci.* **2016**, *166*, 92−99.
(22) Yu, F.; Zhu, C.; Xie, Q.; Wang, Y. Adenosine A2A Receptor Antagonists for Cancer Immunotherapy. *J. Med. Chem.* **2020**, *63*, 12196−12212.
(23) Franco, R.; Cordomí, A.; Llinas del Torrent, C.; Lillo, A.; Serrano-Marín, J.; Navarro, G.; Pardo, L. Structure and Function of Adenosine Receptor Heteromers. *Cell. Mol. Life Sci.* **2021**, *78*, 3957−3968.
(24) Hinz, S.; Navarro, G.; Borroto-Escuela, D.; Seibt, B. F.; Ammon, Y.-C.; de Filippo, E.; Danish, A.; Lacher, S. K.; Červinková, B.; Rafehi, M.; Fuxe, K.; Schiedel, A. C.; Franco, R.; Müller, C. E. Adenosine A2A Receptor Ligand Recognition and Signaling Is Blocked by A2B Receptors. *Oncotarget* **2018**, *9*, 13593−13611.
(25) Majellaro, M.; Jespers, W.; Crespo, A.; Núñez, M. J.; Novio, S.; Azuaje, J.; Prieto-Díaz, R.; Gioé, C.; Alispahic, B.; Brea, J.; Loza, M. I.; Freire-Garabal, M.; Garcia-Santiago, C.; Rodríguez-García, C.; García-Mera, X.; Caamaño, O.; Fernandez-Masaguer, C.; Sardina, J. F.; Stefanachi, A.; El Maatougui, A.; Mallo-Abreu, A.; Åqvist, J.; Gutiérrez-de-Terán, H.; Sotelo, E. 3,4-Dihydropyrimidin-2(1H)-Ones as Antagonists of the Human A2B Adenosine Receptor: Optimization, Structure−Activity Relationship Studies, and Enantiospecific Recognition. *J. Med. Chem.* **2021**, *64*, 458−480.
(26) Franco, R.; Rivas-Santisteban, R.; Navarro, G.; Reyes-Resina, I. Adenosine Receptor Antagonists to Combat Cancer and to Boost Anti-Cancer Chemotherapy and Immunotherapy. *Cell* **2021**, *10*, 2831−2844.
(27) Müller, C. E.; Baqi, Y.; Hinz, S.; Namasivayam, V. Medicinal Chemistry of A2B Adenosine Receptors. *Receptors* **2018**, *34*, 137−168.
(28) Jiang, J.; Seel, C. J.; Temirak, A.; Namasivayam, V.; Arridu, A.; Schabikowski, J.; Baqi, Y.; Hinz, S.; Hockemeyer, J.; Müller, C. E. A2B Adenosine Receptor Antagonists with Picomolar Potency. *J. Med. Chem.* **2019**, *62*, 4032−4055.
(29) Crespo, A.; El Maatougui, A.; Biagini, P.; Azuaje, J.; Coelho, A.; Brea, J.; Loza, M. I.; Cadavid, M. I.; García-Mera, X.; Gutiérrez-De-Terán, H.; Sotelo, E. Discovery of 3,4-Dihydropyrimidin-2(1H)-Ones as a Novel Class of Potent and Selective A2B Adenosine Receptor Antagonists. *ACS Med. Chem. Lett.* **2013**, *4*, 1031−1036.
(30) El Maatougui, A.; Azuaje, J.; González-Gómez, M.; Miguez, G.; Crespo, A.; Carbajales, C.; Escalante, L.; García-Mera, X.; Gutiérrez-De-Terán, H.; Sotelo, E. Discovery of Potent and Highly Selective A2B Adenosine Receptor Antagonist Chemotypes. *J. Med. Chem.* **2016**, *59*, 1967−1983.
(31) Mallo-Abreu, A.; Prieto-Díaz, R.; Jespers, W.; Azuaje, J.; Majellaro, M.; Velando, C.; García-Mera, X.; Caamaño, O.; Brea, J.; Loza, M. I.; Gutiérrez-De-Terán, H.; Sotelo, E. Nitrogen-Walk Approach to Explore Bioisosteric Replacements in a Series of Potent A2B Adenosine Receptor Antagonists. *J. Med. Chem.* **2020**, *63*, 7721−7739.
(32) Vidal, B.; Nueda, A.; Esteve, C.; Domenech, T.; Benito, S.; Reinoso, R. F.; Pont, M.; Calbet, M.; López, R.; Cadavid, M. I.; Loza, M. I.; Cárdenas, Á.; Godessart, N.; Beleta, J.; Warrellow, G.; Ryder, H. Discovery and Characterization of 4′-(2-Furyl)-N-Pyridin-3-Yl-4,5′-Bipyrimidin-2′-Amine (LAS38096), a Potent, Selective, and Efficacious A2B Adenosine Receptor Antagonist. *J. Med. Chem.* **2007**, *50*, 2732−2736.
(33) Mallo-Abreu, A.; Majellaro, M.; Jespers, W.; Azuaje, J.; Caamaño, O.; García-Mera, X.; Brea, J. M.; Loza, M. I.; Gutiérrez-De-Terán, H.; Sotelo, E. Trifluorinated Pyrimidine-Based A2B Antagonists: Optimization and Evidence of Stereospecific Recognition. *J. Med. Chem.* **2019**, *62*, 9315−9330.
(34) Carbajales, C.; Azuaje, J.; Oliveira, A.; Loza, M. I.; Brea, J.; Cadavid, M. I.; Masaguer, C. F.; García-Mera, X.; Gutiérrez-De-Terán, H.; Sotelo, E. Enantiospecific Recognition at the A2B Adenosine Receptor by Alkyl 2-Cyanoimino-4-Substituted-6-Methyl-1,2,3,4-Tetrahydropyrimidine-5-Carboxylates. *J. Med. Chem.* **2017**, *60*, 3372−3382.
(35) Wang, X.; Jespers, W.; Prieto-Díaz, R.; Majellaro, M.; IJzerman, A. P.; van Westen, G. J. P.; Sotelo, E.; Heitman, L. H.; Gutiérrez-de-Terán, H. Identification of V6.51L as a Selectivity Hotspot in Stereoselective A2B Adenosine Receptor Antagonist Recognition. *Sci. Rep.* **2021**, *11*, 1−10.
(36) Tay, A. H. M.; Prieto-Díaz, R.; Neo, S.; Tong, L.; Chen, X.; Carannante, V.; Önfelt, B.; Hartman, J.; Haglund, F.; Majellaro, M.; Azuaje, J.; Garcia-Mera, X.; Brea, J. M.; Loza, M. I.; Jespers, W.; Gutierrez-De-Teran, H.; Sotelo, E.; Lundqvist, A. A2B Adenosine Receptor Antagonists Rescue Lymphocyte Activity in Adenosine-Producing Patient-Derived Cancer Models. *J. Immunother. Cancer* **2022**, *10*, 4592−4592.
(37) *RDKit*.
(38) Fernández-Dueñas, V.; Gómez-Soler, M.; Jacobson, K. A.; Kumar, S. T.; Fuxe, K.; Borroto-Escuela, D. O.; Ciruela, F. Molecular Determinants of A2AR−D2R Allosterism: Role of the Intracellular Loop 3 of the D2R. *J. Neurochem.* **2012**, *123*, 373−384.

https://doi.org/10.1021/acs.jmedchem.2c01768
J. Med. Chem. 2023, 66, 890−912

(39) Xu, Y.; Xie, X.; Duan, Y.; Wang, L.; Cheng, Z.; Cheng, J. A Review of Impedance Measurements of Whole Cells. *Biosens. Bioelectron.* **2016**, *77*, 824−836.
(40) Linden, J.; Thai, T.; Figler, H.; Jin, X.; Robeva, A. S. Characterization of Human A_{2B} Adenosine Receptors: Radioligand Binding, Western Blotting, and Coupling to $G_q$in Human Embryonic Kidney 293 Cells and HMC-1 Mast Cells. *Mol. Pharmacol.* **1999**, *56*, 705.
(41) Kenakin, T. Quantifying Biological Activity in Chemical Terms: A Pharmacology Primer To Describe Drug Effect. *ACS Chem. Biol.* **2009**, *4*, 249−260.
(42) Atwood, B. K.; Lopez, J.; Wager-Miller, J.; Mackie, K.; Straiker, A. Expression of G Protein-Coupled Receptors and Related Proteins in HEK293, AtT20, BV2, and N18 Cell Lines as Revealed by Microarray Analysis. *BMC Genomics* **2011**, *12*, 14−28.
(43) Klotz, K.-N. Adenosine Receptors and Their Ligands. *Naunyn-Schmiedeberg's Arch. Pharmacol.* **2000**, *362*, 382−391.
(44) ClinicalTrials.gov https://clinicaltrials.gov/ct2/results?cond=&term=a2b+adenosine+cancer&cntry=&state=&city=&dist= (accessed 2022−09 -15).
(45) Krenn, W.; Verdino, P.; Uray, G.; Faber, K.; Kappe, C. O. Determination of Absolute Configuration in 4-Aryl-3,4-Dihydro-2(1H)-Pyrimidones by High Performance Liquid Chromatography and CD Spectroscopy 1. *Chirality* **1999**, *11*, 659−662.
(46) Crespo, A.; El Maatougui, A.; Azuaje, J.; Escalante, L.; Majellaro, M.; Loza, M. I.; Brea, J.; Cadavid, M. I.; Gutiérrez-de-Terán, H.; Sotelo, E. Exploring the Influence of the Substituent at Position 4 in a Series of 3,4-Dihydropyrimidin-2(1H)-One A2B Adenosine Receptor Antagonists. *Chem. Heterocycl. Compd.* **2017**, *53*, 316−321.
(47) Guengerich, F. P.; Waterman, M. R.; Egli, M. Recent Structural Insights into Cytochrome P450 Function. *Trends Pharmacol. Sci.* **2016**, *37*, 625−640.
(48) McDonnell, A. M.; Dang, C. H. Basic Review of the Cytochrome P450 System. *J. Adv. Pract. Oncol.* **2013**, *4*, 263−268.
(49) Zhou, Y.; Wang, J.; Gu, Z.; Wang, S.; Zhu, W.; Aceña, J. L.; Soloshonok, V. A.; Izawa, K.; Liu, H. Next Generation of Fluorine-Containing Pharmaceuticals, Compounds Currently in Phase II−III Clinical Trials of Major Pharmaceutical Companies: New Structural Trends and Therapeutic Areas. *Chem. Rev.* **2016**, *116*, 422−518.
(50) Shah, P.; Westwell, A. D. The Role of Fluorine in Medicinal Chemistry. *J. Enzyme Inhib. Med. Chem.* **2007**, *22*, 527−540.
(51) Mastelic-Gavillet, B.; Navarro Rodrigo, B.; Décombaz, L.; Wang, H.; Ercolano, G.; Ahmed, R.; Lozano, L. E.; Ianaro, A.; Derré, L.; Valerio, M.; Tawadros, T.; Jichlinski, P.; Nguyen-Ngoc, T.; Speiser, D. E.; Verdeil, G.; Gestermann, N.; Dormond, O.; Kandalaft, L.; Coukos, G.; Jandus, C.; Ménétrier-Caux, C.; Caux, C.; Ho, P. C.; Romero, P.; Harari, A.; Vigano, S. Adenosine Mediates Functional and Metabolic Suppression of Peripheral and Tumor-Infiltrating CD8+ T Cells. *J. Immunother. Cancer* **2019**, *7*, 1−16.
(52) Saze, Z.; Schuler, P. J.; Hong, C.-S.; Cheng, D.; Jackson, E. K.; Whiteside, T. L. Adenosine Production by Human B Cells and B Cell−Mediated Suppression of Activated T Cells. *Blood* **2013**, *122*, 9−18.
(53) Longo, P. A.; Kavran, J. M.; Kim, M.-S.; Leahy, D. J.Chapter Eighteen - Transient Mammalian Cell Transfection with Polyethylenimine (PEI). In *Methods in Enzymology*; Lorsch, J., Ed.; Academic Press: 2013; Vol. *529*, pp. 227−240.
(54) Taura, J.; Nolen, E. G.; Cabré, G.; Hernando, J.; Squarcialupi, L.; López-Cano, M.; Jacobson, K. A.; Fernández-Dueñas, V.; Ciruela, F. Remote Control of Movement Disorders Using a Photoactive Adenosine A2A Receptor Antagonist. *J. Controlled Release* **2018**, *283*, 135−142.
(55) Taura, J.; Fernández-Dueñas, V.; Ciruela, F.Determination of GPCR-Mediated CAMP Accumulation in Rat Striatal Synaptosomes. In *Receptor and Ion Channel Detection in the Brain: Methods and Protocols*; Luján, R., Ciruela, F., Eds.; Springer New York: New York, NY, 2016; pp. 455−463.
(56) Leff, P.; Dougall, I. G. Further Concerns over Cheng-Prusoff Analysis. *Trends Pharmacol. Sci.* **1993**, *14*, 110−112.
(57) Solly, K.; Wang, X.; Xu, X.; Strulovici, B.; Zheng, W. Application of Real-Time Cell Electronic Sensing (RT-CES) Technology to Cell-Based Assays. *Assay Drug Dev. Technol.* **2004**, *2*, 363−372.
(58) Stallaert, W.; Dorn, J. F.; van der Westhuizen, E.; Audet, M.; Bouvier, M. Impedance Responses Reveal B2-Adrenergic Receptor Signaling Pluridimensionality and Allow Classification of Ligands with Distinct Signaling Profiles. *PLoS One* **2012**, *7*, No. e29420.
(59) Hillger, J. M.; Schoop, J.; Boomsma, D. I.; Eline Slagboom, P.; IJzerman, A. P.; Heitman, L. H. Whole-Cell Biosensor for Label-Free Detection of GPCR-Mediated Drug Responses in Personal Cell Lines. *Biosens. Bioelectron.* **2015**, *74*, 233−242.
(60) Núñez, F.; Taura, J.; Camacho, J.; López-Cano, M.; Fernández-Dueñas, V.; Castro, N.; Castro, J.; Ciruela, F. PBF509, an Adenosine A2A Receptor Antagonist With Efficacy in Rodent Models of Movement Disorders. *Front. Pharmacol.* **2018**, *9*, 1−10.
(61) Motulsky, H. J.; Brown, R. E. Detecting Outliers When Fitting Data with Nonlinear Regression − a New Method Based on Robust Nonlinear Regression and the False Discovery Rate. *BMC Bioinf.* **2006**, *7*, 123−123.
(62) Šícho, M.; Stork, C.; Mazzolari, A.; de Bruyn Kops, C.; Pedretti, A.; Testa, B.; Vistoli, G.; Svozil, D.; Kirchmair, J. FAME 3: Predicting the Sites of Metabolism in Synthetic Compounds and Natural Products for Phase 1 and Phase 2 Metabolic Enzymes. *J. Chem. Inf. Model.* **2019**, *59*, 3400−3412.
(63) Rydberg, P.; Gloriam, D. E.; Olsen, L. The SMARTCyp Cytochrome P450 Metabolism Prediction Server. *Bioinformatics* **2010**, *26*, 2988−2989.
(64) Dang, N. L.; Hughes, T. B.; Miller, G. P.; Swamidass, S. J. Computational Approach to Structural Alerts: Furans, Phenols, Nitroaromatics, and Thiophenes. *Chem. Res. Toxicol.* **2017**, *30*, 1046−1059.
(65) Lu, C.; Wu, C.; Ghoreishi, D.; Chen, W.; Wang, L.; Damm, W.; Ross, G. A.; Dahlgren, M. K.; Russell, E.; Von Bargen, C. D.; Abel, R.; Friesner, R. A.; Harder, E. D. OPLS4: Improving Force Field Accuracy on Challenging Regimes of Chemical Space. *J. Chem. Theory Comput.* **2021**, *17*, 4291−4300.
(66) Marelius, J.; Kolmodin, K.; Feierberg, I.; Åqvist, J. Q: A Molecular Dynamics Program for Free Energy Calculations and Empirical Valence Bond Simulations in Biomolecular Systems. *J. Mol. Graphics Modell.* **1998**, *16*, 213−225.
(67) Jespers, W.; Esguerra, M.; Åqvist, J.; Gutiérrez-De-Terán, H. Qligfep: An Automated Workflow for Small Molecule Free Energy Calculations in Q. *Aust. J. Chem.* **2019**, *11*, 1−16.
(68) Lee, F. S.; Warshel, A. A Local Reaction Field Method for Fast Evaluation of Long-Range Electrostatic Interactions in Molecular Simulations. *J. Chem. Phys.* **1992**, *97*, 3100−3107.
(69) King, G.; Warshel, A. A Surface Constrained All-Atom Solvent Model for Effective Simulations of Polar Solutions. *J. Chem. Phys.* **1989**, *91*, 3647−3661.
(70) Robertson, M. J.; Tirado-Rives, J.; Jorgensen, W. L. Improved Peptide and Protein Torsional Energetics with the OPLS-AA Force Field. *J. Chem. Theory Comput.* **2015**, *11*, 3499−3509.
(71) Banks, J. L.; Beard, H. S.; Cao, Y.; Cho, A. E.; Damm, W.; Farid, R.; Felts, A. K.; Halgren, T. A.; Mainz, D. T.; Maple, J. R.; Murphy, R.; Philipp, D. M.; Repasky, M. P.; Zhang, L. Y.; Berne, B. J.; Friesner, R. A.; Gallicchio, E.; Levy, R. M. Integrated Modeling Program, Applied Chemical Theory (IMPACT). *J. Comput. Chem.* **2005**, *26*, 1752−1780.
(72) Ryckaert, J.-P.; Ciccotti, G.; Berendsen, H. J. C. Numerical Integration of the Cartesian Equations of Motion of a System with Constraints: Molecular Dynamics of n-Alkanes. *J. Comput. Phys.* **1977**, *23*, 327−341.
(73) Wang, L.; Deng, Y.; Knight, J. L.; Wu, Y.; Kim, B.; Sherman, W.; Shelley, J. C.; Lin, T.; Abel, R. Modeling Local Structural Rearrangements Using FEP/REST: Application to Relative Binding

https://doi.org/10.1021/acs.jmedchem.2c01768
J. Med. Chem. 2023, 66, 890−912

Affinity Predictions of CDK2 Inhibitors. *J. Chem. Theory Comput.* **2013**, *9*, 1282−1293.
(74) Hagberg, A.; Swart, P.; S Chult, D. Exploring Network Structure, Dynamics, and Function Using NetworkX. *7th Python Sci. Conf. SciPy* **2008**, *2008*, 11−15.
(75) Wang, L.; Wu, Y.; Deng, Y.; Kim, B.; Pierce, L.; Krilov, G.; Lupyan, D.; Robinson, S.; Dahlgren, M. K.; Greenwood, J.; Romero, D. L.; Masse, C.; Knight, J. L.; Steinbrecher, T.; Beuming, T.; Damm, W.; Harder, E.; Sherman, W.; Brewer, M.; Wester, R.; Murcko, M.; Frye, L.; Farid, R.; Lin, T.; Mobley, D. L.; Jorgensen, W. L.; Berne, B. J.; Friesner, R. A.; Abel, R. Accurate and Reliable Prediction of Relative Ligand Binding Potency in Prospective Drug Discovery by Way of a Modern Free-Energy Calculation Protocol and Force Field. *J. Am. Chem. Soc.* **2015**, *137*, 2695−2703.

https://doi.org/10.1021/acs.jmedchem.2c01768
J. Med. Chem. 2023, 66, 890−912